Sulfuric Acid Corrosion to Simulate Microbial Influenced Corrosion on Stainless Steel 316L

by

Jacob T. Miller

Submitted in Partial Fulfillment of the Requirements

for the Degree of

Master of Science in Engineering

in the

Chemical Engineering

Program

YOUNGSTOWN STATE UNIVERSITY

December, 2017

Sulfuric Acid Corrosion to Simulate Microbial Influenced Corrosion on Stainless Steel 316L

Jacob T. Miller

I hereby release thesis to the public. I understand that this thesis will be made available from the OhioLINK ETD Center and the Maag Library Circulation Desk for public access. I also authorize the University or other individuals to make copies of this thesis as needed for scholarly research.

Signature:

Jacob T. Miller, Student Date

Approvals:

Dr. Holly J. Martin, Thesis Advisor Date

Dr. Pedro Cortes, Committee Member Date

Dr. Brett P. Conner, Committee Member Date

Dr. Salvatore A. Sanders, Dean of Graduate Studies Date

Abstract

The continued improvement of additive manufacturing (3D printing) is progressively eliminating the geometric limitations of traditional subtractive processes. Because parts are built up in thin layers, such as in processes like Laser Powder Bed Fusion, complex parts can be manufactured easily. However, this manufacturing method likely causes the parts to have rougher surfaces and decreased density compared to their traditional counterparts. The effect of this difference has not been researched thoroughly, but may have a significant impact on the properties of the parts. For example, the 3D printed parts could more easily collect micro-organisms that produce sulfuric acid as byproducts of their metabolic processes. Uninhibited microbial growth on the sample surface could produce enough sulfuric acid to degrade the parts through hydrogen embrittlement. This research contrasts the tensile stress and corrosion behavior of 316L stainless steel between traditional and additive manufactured parts based on exposure time to a 0.75 molar sulfuric acid solution, which mimics microbial metabolic byproducts.

Acknowledgements

I am dedicating this thesis to my parents, Mike and Phyllis Miller, and my brothers, Michael and Scott Miller. Their unwavering support and love have allowed me to excel in ways I never thought possible. I owe more to them than I will ever be able to repay.

I would like to thank my advisor, Dr. Holly Martin, for her constant guidance and expertise. The skills she helped to develop in me throughout my time at YSU will undoubtedly follow me in my professional career and beyond.

I wish to thank Dr. Pedro Cortes and Dr. Brett Conner for volunteering their time to be on my committee. Their knowledge and insight were valuable in improving my thesis. I am grateful for Dr. Douglas Price's constant advice and for challenging me to improve my way of thinking over the last six years. I want to thank Dr. Dingqiang Li for helping me to understand the theory and operation of the scanning electron microscopes on campus. My study would not have been possible without the data collected under his supervision. I also wish to thank the numerous faculty members who helped me complete my thesis with their guidance, instruction, and support.

Finally, I wish to thank all of my family members and friends who have provided me with an infallible support system. Whenever times were difficult, I turned to you for support and was never left empty handed. You have all helped shape me as a professional and an individual, and I am humbled by your immeasurable love.

Table of Contents

List of Figures

List of Tables

1.0 Introduction and Literature Review

Since first being mass produced in blast furnaces in the mid-19th century [1], steel has been invaluable to major industries, such as automotive, aerospace, and construction. The production of steel has become more precise and efficient since the introduction of the Bessemer process. Carbon steel, which consists of only iron and carbon, accounts for a majority of steel produced today [2]. However, alloying elements can be added during production to obtain favorable properties in the steel. Elements such as manganese, nickel, molybdenum, and chromium are very common in modern steel alloys. Different combinations of these alloying elements result in steels with varying properties and uses, such as increased creep resistance for steels exposed to high temperatures or increased tensile strength for steels used in construction.

To effectively control the amounts of each alloying element and the overall composition of the steel product, more advanced equipment, such as Electric Arc Furnaces (EAFs), have been developed. Unlike traditional furnaces which use ores and other raw materials to produce steel, EAFs can use scrap metal as the feed stock to produce new product. The scrap metal is loaded into the furnace and an electrode with an electric current running through it is then placed in the furnace. The electric arc produced by the current running through the electrode melts the metal into a molten liquid [1]. Alloying elements can then be added into the batch by weight, allowing the manufacturer to produce batches with the desired composition.

Different alloying elements used in steel products are added to obtain favorable properties depending on the environment and stresses the steel must withstand. For example, manganese is used in small amounts to increase strength of steel products [3].

The addition of nickel helps to increase ductility, as well as improve corrosion resistance against some acids. Rare elements, such as niobium, help prevent inter-granular corrosion, particularly in the heat affected zone (HAZ) after welding. Molybdenum can be used to increase the corrosion resistance of steel to chloride ions [4]. Chromium is often used as an additive in order to promote corrosion resistance in other acidic environments, especially against oxidation in air [4].

Steels containing specified amounts of different alloying elements can be further categorized into groups. Carbon steels and alloy steels are designated with a four digit number; the first digit indicates the main alloying element(s), the second digit indicates the secondary alloying element(s), and the last two digits indicate the amount of carbon, in hundredths of a percent by weight. Traditional carbon steels begin their four digit number with 1, nickel steels with 2, and so on [5]. More specific designations are used for each unique combination. For example, 1060 steel is a plain-carbon steel containing 0.60% carbon by total weight [6].

One such group of particular interest are stainless steels, which are steel alloys containing a minimum of 11% chromium by weight [7]. The chromium passivates in the presence of oxygen to form a thin layer of chromium oxide, which protects the metal underneath [8]. This film reforms even if the surface of the metal is scratched or damaged. Stainless steels are incredibly versatile because they have the strength of typical steel products while also remaining resistant to many corrosive environments.

Stainless steel (SS) can be further categorized into grades, each of which has criteria of alloying elements that must be met. Most stainless steels are given three digit specification numbers which provide information about their composition; however, the

identification numbers themselves do not contain specific alloying information as with the carbon steels described previously. For example, stainless steels in the 200 series, as defined by the Society of Automotive Engineers (SAE), are stainless steels containing chromium, nickel, and manganese [9]. The 500 series contains heat resisting chromium alloys while stainless steels in the 300 series are steels containing at least 16% chromium and 6% nickel by weight [10]. Contained within each series are more specific grades, such as SS 316, which contains 16-18% chromium, 10-14% nickel, 10% nitrogen, 2-3% molybdenum, 2% manganese, and 0.8% carbon by weight [4]. SS 316 is used in environments where both strength and corrosion resistance are required, such as aerospace, pharmaceuticals, cutlery, and marine applications [11]. SS 316L, which has a maximum of 0.3% carbon versus 0.8% in SS 316, is used for improved performance under corrosive environments, especially where potential leaching of carbon from the steel would decrease strength [7].

Stainless steel 316L is used in some industries specifically for its unique combination of strength and corrosion resistance. Small specialized parts for International Thermonuclear Experimental Reactor (ITERs) are designed to operate under high temperatures while maintaining structural integrity [12]. Uses for SS 316 also extend to biomedical implants as both corrosion resistance and strength are vital within the demanding environment of the human body [13].

Issues with SS are found in the actual production process, as well as the machining of the parts afterwards. When exposed to the heat required for welding, the elements within the sample do not remain evenly distributed throughout the part [14]. The alloying elements will disperse preferentially; the welded part itself will not be

harmed mechanically, but a given distance away from the weld, there will be an unequal distribution of the alloying elements in the sample [15]. This localized area, called the heat affected zone (HAZ), can lead to increased corrosion at these weak points and cause the part to fail sooner than predicted. The steel's microstructure can change in the HAZ due to unequal cooling rates, resulting in different grain sizes than the bulk material [14]. Additional problems, such as stress corrosion cracking, can also manifest due to the migration of alloying elements in the HAZ if the SS samples do not have enough chromium present to allow for adequate passivation [15]. Another problem with SS is that traditional production methods have severe limitations on the geometries in which the parts can be manufactured [16]. Many intricate SS parts must undergo extensive welding, machining, and other processes in order for the parts that come out of the furnace to be used. Only simple extrusions like billets, pipes, wires, sheets, etc. are typically capable of being produced straight out of the furnace, and this can limit the uses of SS [17].

One way to help combat both the geometric and mechanistic limitations of SS is by applying additive manufacturing technology to the material, more commonly referred to as three dimensional (3D) printing. The 3D printing processes of many materials have experienced vast improvement in recent years, and these promising developments have expanded the use of 3D printed materials in many industries. One of the many methods of 3D printing materials, Laser Powder Bed Fusion (LPBF), has been gaining popularity and shows potential for further development. The LPBF method of 3D printing begins with the chosen printing material in the form of a dry powder. The powder is laid out in very thin layers, usually around 25 microns thick for metal powders [18]. A laser above the

stage is used to heat the powder until it nearly melts and solidifies, much like the process of forming a weld [19]. In this process, the powder does not melt the same way it would in a furnace or in the more complex Selective Laser Melting (SLM) process [20]. Once the powder solidifies, all loose powder is recycled back into the printer and the stage moves down so that a new layer of powder can be applied above the new solid layer. This process is repeated, which builds up the product layer by layer with the geometries of the product. LPBF development will give manufacturers the ability to print out a single metal part with intricate geometries that would be impossible to produce using traditional machining techniques, as well as eliminating nearly all wasted material typically produced in traditional machining processes [21].

However, even with these promising advantages, 3D printed materials still have their weaknesses. One of the major drawbacks in using 3D printed materials stems from the manufacturing process. The metal powder is not melted down in the same way that traditional stainless steel is in an Electric Arc Furnace. The laser used to "melt" the individual layers of the 3D printed part can cause these parts to be more porous, less dense, or have other altered physical properties compared to their traditionally manufactured (TM) counterparts [22]. A different mechanism of cooling takes place during the LPBF process in which the laser power, the speed at which the laser moves across the stage, and even the process used to produce the powder used to make the parts will all impact the properties of the final product [23, 24]. On a smaller scale, this difference in production also causes the molecules in the metal to arrange themselves differently [25]. The higher temperature and extended period of time the metal spends in the Electric arc furnace allows the molecules to orient themselves in a stable

confirmation. However, the 3D printed powder that builds up layer by layer is unable to do this. The partially melted powder can only interact with the solid layer of material beneath it. This limits the amount of time the molecules have to rearrange from the high energy state caused by the laser. Without the extra time to rearrange, the molecules in the 3D printed parts may be "stuck" in a higher energy state and, therefore, a higher stressed orientation than the traditionally manufactured parts [26]. The powder in 3D printed samples can only orient with the layer underneath it while TM samples can come to a lower energy state with respect to all of the surrounding molecules since they are all cooling at the same time [12].

The differences in density and molecular orientation caused by 3D printing have an impact on the physical and mechanical properties of the TM vs 3D parts as well. 3D samples have shown decreased values in tensile stress and stain compared to samples produce using traditional methods [27]. Corrosion resistance is another property that could be affected by the molecular orientation caused by 3D printing and must be accounted for when choosing a material to be placed in a given environment. The corrosive environment that the samples are exposed to also impacts the type of corrosion which takes place, as well as the damage sustained by the samples [28]. As an example, one of the possible uses for 3D printed SS 316L is hydrogen storage vessels, as both volume and reliability are necessary for safety [29]. Hydrogen stored to use for fuel must be kept at high pressures in order to be economically viable; however, storing hydrogen in this way creates an environment that may induce corrosion. Hydrogen embrittlement (HE), a mechanism which can result in plastic deformation and weakening of mechanical properties, can take place in conditions with a high enough concentration of hydrogen

ions [30]. Additionally, environments containing chloride ions are incompatible with SS and can cause significant damage [31]. Accounting for hydrogen embrittlement and corrosion are necessary for the use of stainless steels in any environments designated of potential use.

Proposed treatments of stainless steels to further improve corrosion resistance are well documented. Treatments such as nitriding, which is diffusing nitrogen into the surface of a metal, have been found to affect the properties of stainless steels. Formation of nitride precipitates increased surface hardness of the samples [32]. Depending on the temperature of this process, however, nitriding negatively impacted corrosion resistance [3]. More complex treatments, such as glow-discharge nitriding, were able to increase the hardness of stainless steel samples by a factor of four [33]. However, the complex nature of these treatments must still be developed and tested using 3D printed substrates.

Environments with constant concentrations of corrosive ions such as those present in hydrogen storage or with chloride ions are known to be harmful for 3D SS products. Additionally, in many cases, these products may also be exposed to varying concentrations of corrosive ions caused by the metabolic processes of living organisms. Specifically, microbial influenced corrosion (MIC) can cause significant damage to manufactured products if the environment allows for the microbes to thrive [34]. In the 3D printed samples, the characteristically rough surface [35] can provide protection for the microbes, allowing them to reproduce, metabolize more frequently, and, in the case of sulfur oxidizing bacteria (SOB), produce larger amounts of corrosive byproducts [34]. The unpredictability of microbial behavior also impacts the amount of damage they can cause to a given sample. This unpredictability in many cases leads to increased localized

damage of a sample, unlike an abiotic system, where no living organisms are present and the corrosive ion concentrations are essentially constant [36]. A 2015 study by Usher et all describes some of the challenges in measuring MIC on SS 316L [37]. Some studies have been performed trying to better predict the behavior of microbes and quantify the damage caused by corrosive microbial byproducts. The electrochemical noise technique, defined as the random fluctuations of the potential and current passing through an interface, can give information about the kinetics and mechanisms as a sample corrodes. Changes in the current passing through a system containing samples in a corrosive environment can produce information about the type of corrosion mechanisms taking place as well as the speed at which it occurs [38]. The signals collected through this technique can indicate if the samples have experienced damage due to MIC before the damage would be visible by other measurement methods, such as optical microscopy. Early detection of MIC is important because if the microbes causing damage are not identified and removed, they will be able to multiply and corrode the samples more rapidly [34]. Another complication with MIC comes with the complex nature of the microbes themselves. Microbial communities are commonly made up of a mix of different bacterial isolates, making it even more difficult to attribute the damage caused by MIC to any individual type of microbe. Due to their diverse nature, microbial communities are also able to cause more damage than pure cultures through MIC [37].

Damage caused by MIC is difficult to observe and quantify; however, advanced instruments such as a Scanning Electron Microscopes (SEM) can be used to analyze samples with excellent precision and clarity [39]. Unlike an optical microscope, which directs reflected light through lenses to produce an image, a SEM uses a laser to direct

electrons through electromagnetic lenses, focusing the electrons into a beam which is used to scan the sample. The entire system must be kept under a vacuum in order to prevent oxidation of the filament in the laser and to ensure the electrons do not interact with air molecules before reaching the sample surface [40]. The electrons that contact the sample excite electrons within the sample causing them to emit as high energy backscattered electrons or lower energy secondary electrons [41]. Special instrumentation is used to "catch" these emitted electrons and different probes interact with computer software to produce clear images of the sample. Very high resolution images can be obtained because the limit of detection is much lower using electrons as opposed to using light to scan the samples [40]. Detailed images obtained through SEM analysis can be used to detect damage caused by MIC sooner than visual inspection or optical microscopy. SEM imaging of 3D and TM samples exposed to environments where MIC occurs could be used to observe differences in the surface features and support differences in physical properties of the samples.

Because there is a clear difference between the tensile stress and strain of 3D vs TM products [27, 42], then a difference in the chemical and physical properties between the parts is reasonable. Determining the difference in these properties between samples is essential if 3D parts ever hope to replace TM parts in industrial applications. SEM images of 316L SS samples produced using 3D and TM methods could help quantify these differences and outline potential areas of improvement in the manufacturing process. The methods and results following quantify the differences in corrosion resistance of 3D and TM samples in a corrosive environment, which mimics the byproducts produced by SOBs. The 3D samples will likely experience more damage due

to their characteristically rough surface and increased residual stress, giving the corrosive ions more locations to attack and degrade the samples compared to their TM counterparts. If more damage is sustained by the 3D samples than the TM samples as hypothesized, the resulting degradation of physical properties should also increase in the 3D samples. Knowing the degree of damage sustained by 3D samples versus their TM counterparts will help determine the necessary production improvements required before 3D products will be able to safely replace TM products, especially in variably corrosive environments.

2.0 Materials and Method

2.1 Sample Preparation

3D printed 316L Stainless Steel samples were produced using Laser Powder Bed Fusion (LPBF) by the public-private partnership America Makes, located in downtown Youngstown. A Renishaw 250AM printer with a continuous wave Ytterbium fiber laser was used to create the 3D samples at a build rate of approximately 20cm^3/hr. The laser ran at 200 Watts in a modulated operation pulsed with a TTL trigger, allowing for more stable melting of the powder than continuous laser scanning. Excess material, namely the supports necessary to build the parts, was carefully removed using small vice grips, being sure not to compromise the gage thickness or gage width of the samples. The samples were then measured using calibers to verify that the dimensions of the actual samples were similar to those from the STL file. The traditionally manufactured steel samples were cut using the same measurements from the STL file using a sheet of 316L stainless steel. Twenty-seven samples using each manufacturing process were produced, with the dimensions shown in Figure 1. No surface treatments were applied to either the 3D or traditionally manufactured samples.

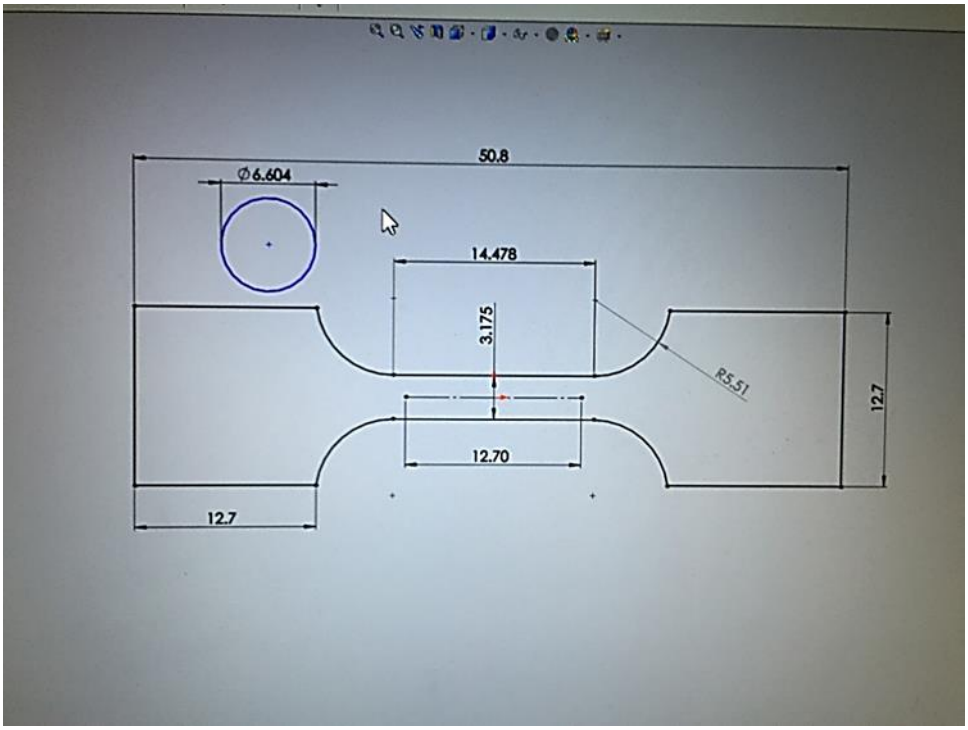

Figure 1 shows the dimensions from the STL file used to produce the 3D printed samples (all measurements in millimeters). 3D printed samples were produced using an LPBF method and uploading the appropriate dimensions of the STL file to the printer. Dimensions are scaled down from ASTM E-8 standards for dog bone shaped samples used in tensile testing [43]. The samples were reduced in size to produce a larger quantity of samples, to save on material costs, and to allow for the collection of statistically significant data. The traditionally manufactured samples were cut to the same dimensions from a sheet of metal with the same composition as the powder used for the 3D printed samples.

2.2 Corrosion Testing

The samples were placed in identical 3-quart Pyrex dishes filled with 2 liters of a 0.75M sulfuric acid solution to mimic the environment caused by microbes as described in Okabe et. all and covered with plastic wrap [34]. To create this solution, 80mL of 96% sulfuric acid (Acros Organic, New Jersey) were added to 1920mL of deionized water. All samples were completely immersed in the sulfuric acid solution. The two dishes were used to separate the samples by production method, in an effort to prevent the possibility of galvanic corrosion due to the potential of differences in surface compositions. The solution was drained and replaced every seven days to control the amount of corrosive ions in the solution and to combat the evaporation of the solution.

2.3 Surface Characteristic Examination

After one day of exposure to the sulfuric acid solution, all of the traditional manufactured and additive manufactured (3D printed) samples were removed from the solution. Three samples of each production method were designated for additional testing, while the rest of the samples were placed back into the solution. The remaining samples were removed and tested after 96, 168, 334, 668, 1176, 1680, and 2184 hours of exposure time, leaving fewer samples left to be placed back into solution with the same testing, outlined below, after each removal. Additionally, a longitudinal study was performed using the last group of samples to be permanently removed from the solution. Mass, dimensions, and micrographs using an optical microscope (Nikon SMZ800, software: μscope essentials version 22.1x64, PixelLink, Ottawa, ON, Canada) of the surface of this group of samples were taken at each time an earlier group was removed for additional testing.

2.4 Mechanical Testing

After removing a set of samples of each type from their solutions, the samples were rinsed off individually using DI water. The samples were then dried with paper towels and left to air dry for 10 minutes. The samples were then measured with calipers (Harbor Freight) to determine their gage width, length, and thickness. A laboratory grade balance (SI-234, Denver Instrument, NY) was used to determine the mass of each sample. Each sample was then put through a single axial tensile test using an INSTRON with a 150kN load cell (model 5500R using Bluehill 3 software, version 3.61, Illinois Toolworks, IL). The samples were placed in the grips of the machine, the extension rate was set to 1 mm/min, and the test was run until the sample fractured. The tensile stress and strain at the point of fracture were then calculated for each sample, using the load and extension data gathered during the experiment. The three data points for each sample type were averaged to obtain strain and tensile stress values for each sample type after a certain amount of exposure time in the sulfuric acid solution.

2.5 Graphical Analysis

After the samples were fractured from the tensile testing, the fracture surfaces of the samples were then analyzed using the available Scanning Electron Microscopes (SEM) on campus. First, the fractured samples were cleaned using a sonicator (M2800 Bransonic series, Branson Ultrasonics Coorperation, CT). Each sample to be analyzed was placed in a 100mL glass jar filled with 25mL acetone. This solvent was chosen because it will not react with the metal chemically, so sonication would only remove loose material and keep the integrity of the fracture surface. The sonicator was filled with

500 mL of water, the glass jars were placed in the sonicator, the timer on the sonicator was set for 10 minutes, and the samples were left to be cleaned. After sonication, the samples were removed from the jars and allowed to air dry for 20 minutes to ensure complete evaporation. Afterwards, the samples were sealed in small plastic bags to protect them from further damage. They remained in the bags until they were examined under the SEM.

The SEM systems used to obtain the images were a Jeol brand JSM-IT300LV and a JIB 4500 multi beam system (Jeol, MA). For either system, the window to the SEM was vented to the atmosphere, as it is held under vacuum when not in use. Next, the stage is removed from the window and the samples were secured to it using double coated carbon conductive tape, with caution taken to prevent contamination from dust, oils, or water. The samples were placed vertically on the stage with the fractured side of each sample facing upward. The height of the samples above the stage must be measured to make sure that the samples will clear the door to the window of the SEM. Once these precautions have been taken, the stage was secured in the window, the door to the window was shut, and a vacuum was pulled on the system. After the appropriate vacuum pressure has been reached, the electron beam is turned on in the chamber. The stage is then moved so that the samples are very close to the source of the electron beam using the controls available from the software. The working distance for all of the images taken was kept between 10 and 25mm. The scale bars present on each image also allow for comparisons to be made by helping the viewer correct for distortion caused by taking images at varying magnifications.

Once the distance between the sample and the electron beam have been set, the magnification and focus of the image were manipulated to obtain a clear image of the sample. Then, the magnification was increased, and the focus was altered again. This process repeated until the image was as clear as possible at a magnification twice as large as the highest magnification desired for analysis. No images were taken as the focus was being adjusted. Once the final focus was obtain, the magnification was reduced and screenshots were taken at each desired magnification. The focus was changed to be as clear as possible at 20000x magnification, and images were taken for each sample at magnifications of 10000, 5000, 500, and 33 times magnification. These levels of magnification were chosen to show both the fracture surface as a whole and a close up view of each sample. Other variables such as the pitch, contrast, and brightness were altered to obtain clearer images. Pitch was only used occasionally to help steady the image for a given magnification. Brightness and contrast were altered to ensure that the surface features in each sample were clearly visible, being careful not to make the images too bright and cause distortions.

All of the samples loaded on the stage were analyzed in this way; no more than six samples were put on the stage at once for analysis. Once all of the images were taken, the stage was moved away from the electron beam and back to its original position in the window. The electron beam was deactivated as it was no longer in use. The vacuum in the system was then slowly vented to the atmosphere, and after completion, the door to the window was opened and the stage was removed. The window was then closed again and the vacuum was pulled on the system. The images were saved as TIF files to preserve all of the data available and later analyzed after all of the images had been collected.

2.6 Density Testing

After fracture, the volume of the samples was determined using the Archimedes method of water displacement. Note that testing density before or after fracturing the samples will not affect the results; the samples were not fractured until after they were exposed to the sulfuric acid solution for the required amount of time. First, the samples were weighed while dry using a balance (SI-234, Denver Instrument, NY). Then, both pieces of the broken samples were placed into 25mL graduated cylinders filled with a pre-measured volume of water (15mL). After the samples were placed in the cylinders, the initial volume increase was recorded. Water was then added to the cylinders until the graduated cylinders were completely filled. The graduated cylinders were then covered with Parafilm in order to prevent evaporation of the water. The samples remained submerged for 72 hours in order to allow for the water to penetrate the samples. After this time, the samples were removed while the water in the full 25mL graduated cylinder was poured out into a 50mL graduated cylinder and the total volume of water was recorded. The volume above the 25mL mark of the graduated cylinders was measured so that when the full 25mL graduated cylinders were emptied, the total remaining volume would be known. This way, the total volume removed along with the initial volume increase caused by the sample would be used to determine the final volume of the samples. Once removed, the samples were weighed immediately while "wetted". The difference in dry mass versus wetted mass and the determined volume of the samples were used to calculate density.

3.0 Results

Figure 2 shows micrographs of the traditionally manufactured (top row) and 3D printed (bottom row) samples before being exposed to the sulfuric acid solution. Scale bars are provided to allow for accurate measurement of surface features. Much smoother surfaces were observed on the traditionally manufactured samples than their 3D printed counterparts. The Laser Powder Bed Fusion (LPBF) process used to produce the 3D samples does not allow the molecules to rearrange into the most stable configuration. This causes residual stress within the samples as well as their rough texture compared to the traditionally manufactured samples.

Figure 3 shows micrographs of the traditionally manufactured (top row) and 3D printed (bottom row) samples after 2184 hours of exposure in the sulfuric acid solution. The grains are more clearly defined in the 3D samples than in the traditionally manufactured samples. The surfaces of both sample types show signs of corrosion and mass loss, but more damage is observed on the 3D samples, as shown by the arrows present in the images. The rough grooves on the surface highlighted by the arrows on the 3D image are more defined than the grooves in the TM images.

Figure 4 shows the mass loss (in grams) of both 3D printed and traditionally manufactured samples as a function of exposure time (in hours). Samples of both production methods show positive linear trends, but the 3D samples show rates of mass loss nearly three times greater than their traditionally manufactured counterparts. The mass lost from the 3D samples increases with exposure time, but the mass lost from the traditionally manufactured samples stagnates after 672 hours of exposure time. The error bars present represent one standard deviation. In the 3D samples, the deviations increase

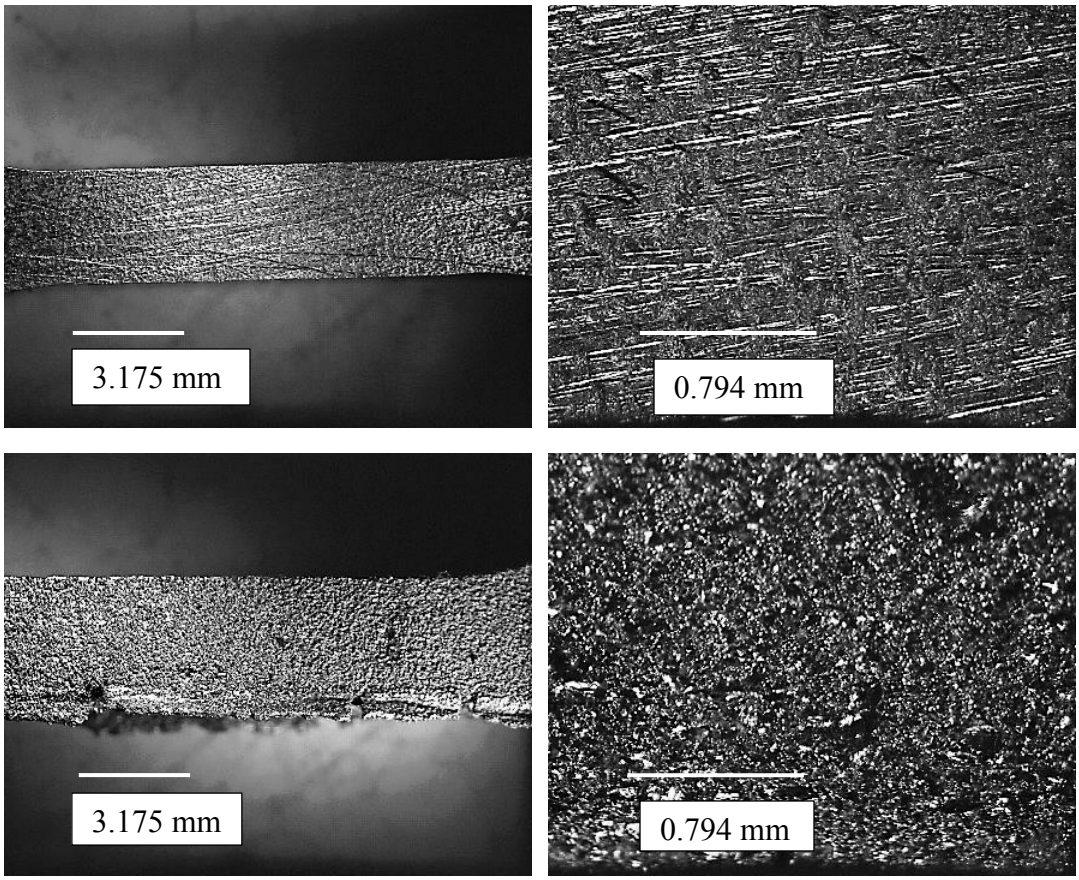

Figure 2 shows micrographs of the traditionally manufactured (top row) and 3-D printed (bottom row) samples before being exposed to the sulfuric acid solution. Scale bars are provided to allow for accurate measurement of surface features.

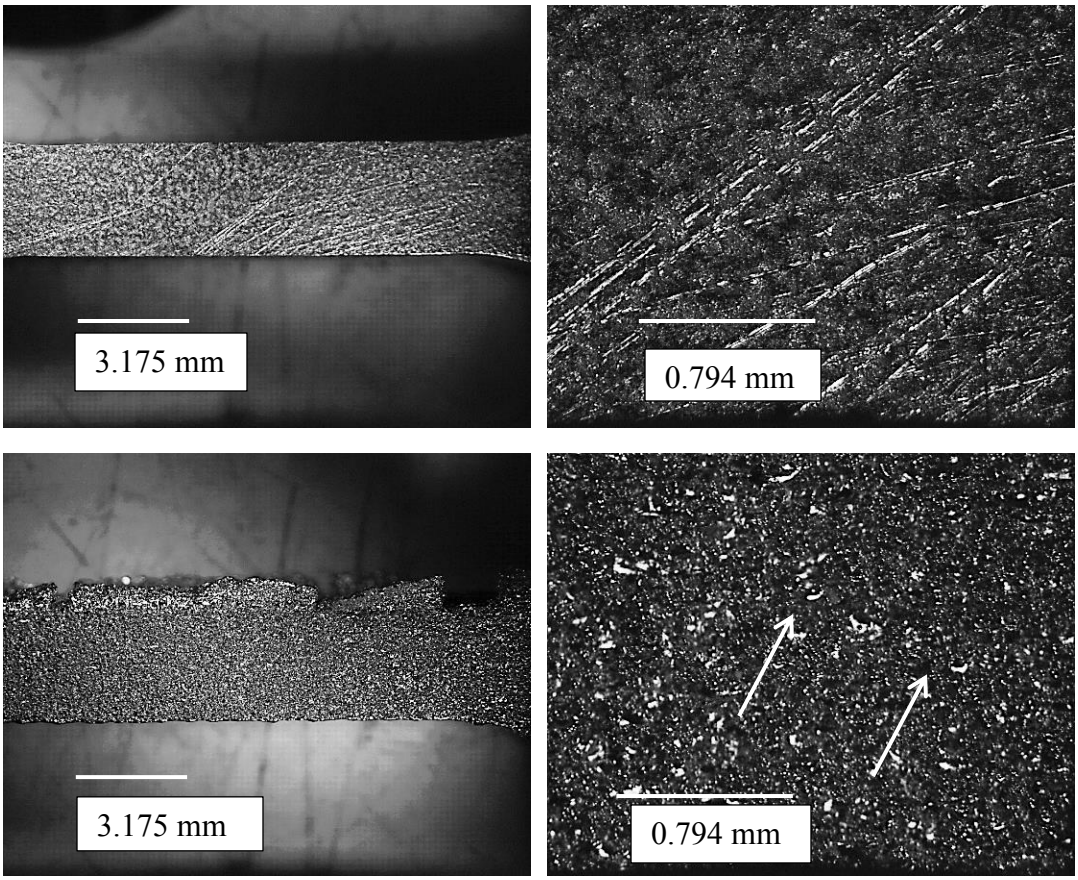

Figure 3 shows micrographs of the traditionally manufactured (top row) and 3-D printed (bottom row) samples after 2184 hours of exposure in the sulfuric acid solution. The surfaces of both samples types show signs of corrosion and mass loss, but more damage is observed on the 3-D samples as shown by the arrows present in the images.

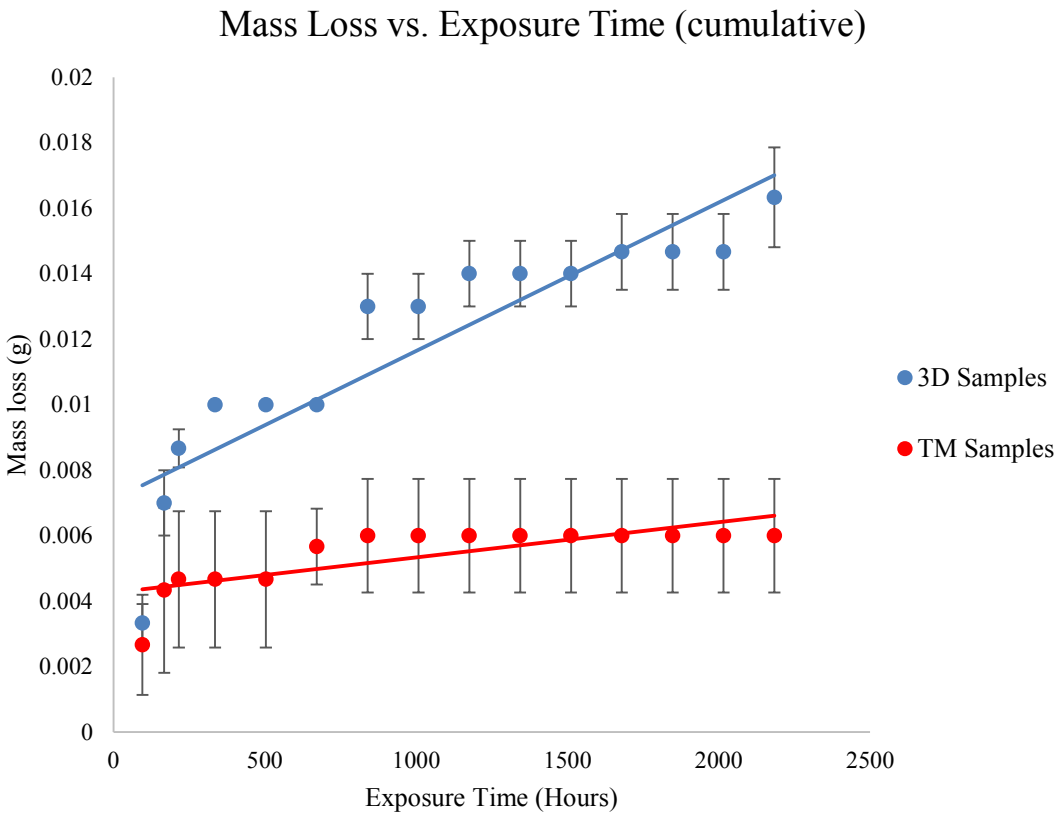

Figure 4 shows the mass loss (in grams) of both 3D printed and traditionally manufactured samples as a function of exposure time (in hours). Samples of both production methods show positive linear trends, but the 3D samples show rates of mass loss nearly three times greater than their traditionally manufactured counterparts.

slightly as the total amount of mass loss increases. The error bars of the TM samples are essentially constant in size because the amount of mass loss no longer increased after approximately 850 hours of exposure time.

Figure 5 shows the density of both the 3D and TM samples (in g/mL) as a function of exposure time (hours). The density of both the 3D and TM samples remain nearly constant as exposure time in the sulfuric acid solution increases. Error bars represent one standard deviation. The error bars are consistent in size between the 3D and TM samples, and the large size of the error bars is due to the variations in mass and volume between individual samples.

Figure 6 shows tensile stress (in MPa) of both the 3D printed and traditionally manufactured samples as a function of exposure time (in hours). While a negative linear relationship is observed between tensile stress and exposure time with the 3D printed samples, the tensile stress remains essentially constant for the traditionally manufactured samples. Unintentional torque was likely applied to one of the 3D samples exposed for 1680 hours, resulting in the large standard deviation present. However, this point does not impact the trend of the data overall. The error bars present represent one standard deviation. More variation was present in the tensile stress of the 3D samples as exposure time increased, resulting in the large error bars. The tensile stress of the TM samples show much less variation than the 3D samples and, in turn, has much smaller error bars.

Figure 7 shows strain (in mm/mm) of both the 3D printed and traditionally manufactured samples as a function of exposure time (in hours). A negative trend is observed between strain and exposure time with the 3D printed samples, specifically after 1176 hours of exposure time in the corrosive environment. The strain of the traditionally

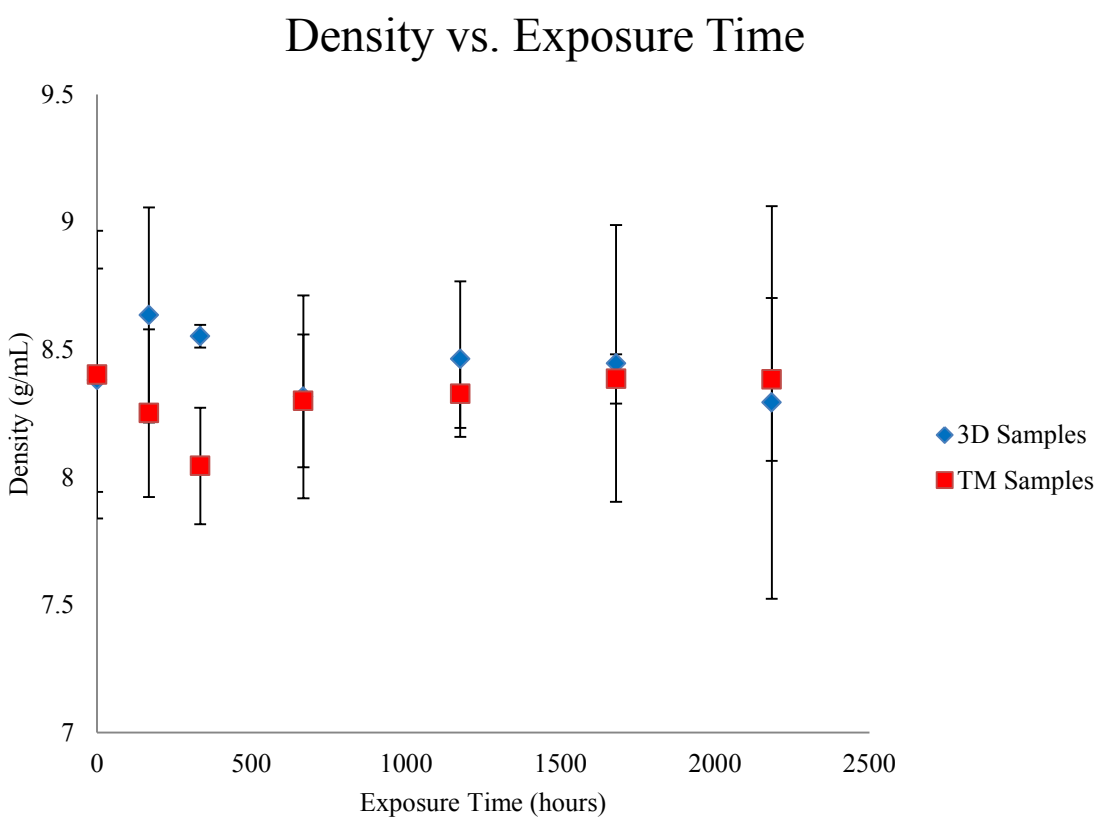

Figure 5 shows the density (g/mL) of the 3D and TM samples as a function of exposure time (hours) in the sulfuric acid solution. Density of both the 3D and TM samples stay essentially constant as exposure time increases.

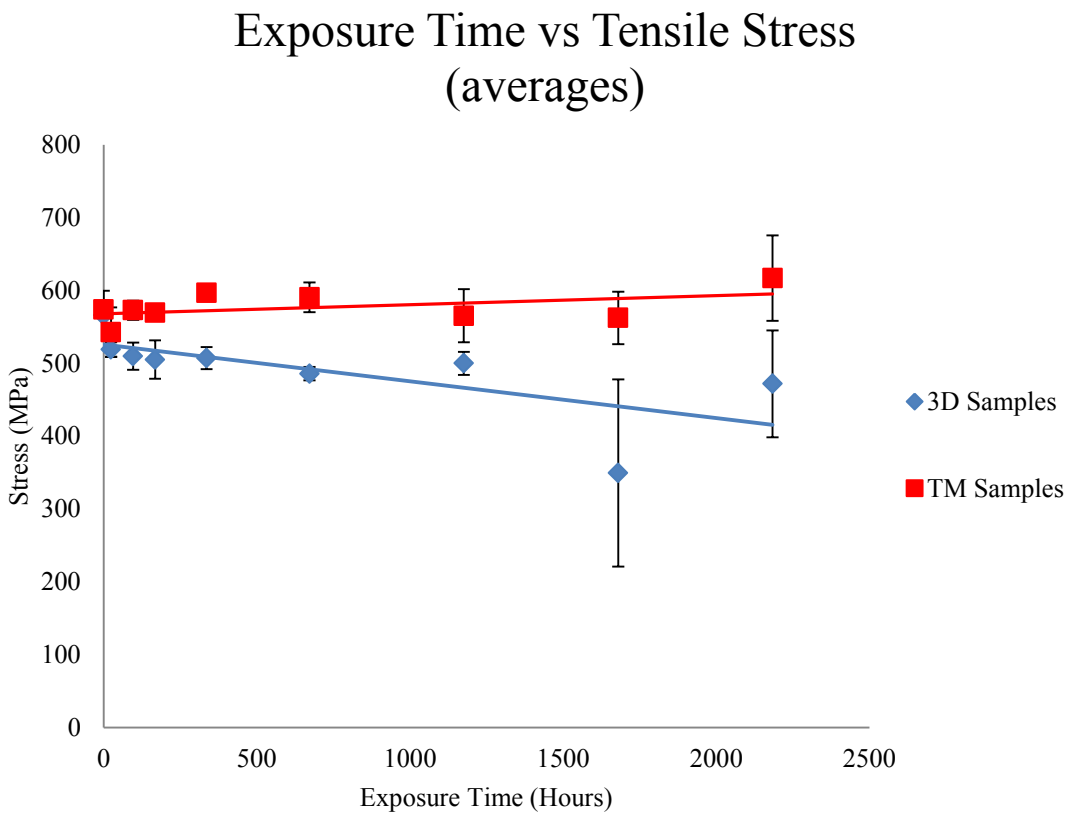

Figure 6 shows tensile stress (in MPa) of both the 3D printed and traditionally manufactured samples as a function of exposure time (in hours). While a negative linear relationship is observed between tensile stress and exposure time with the 3D printed samples, the tensile stress remains essentially constant for the traditionally manufactured samples.

manufactured samples remained essentially constant, even with prolonged exposure. The error bars present represent one standard deviation. More variation was present in the strain of the 3D samples as exposure time increased, resulting in the large error bars. The strain of the TM samples show much less variation than the 3D samples and, in turn, has much smaller error bars.

Figure 8 shows the stress strain curve for the 3D and TM samples at 0 and 2184 hours of exposure time in the sulfuric acid solution. The TM samples demonstrated higher values of tensile stress than the 3D samples when comparing the controls. After 2184 hours of exposure time, the tensile stress of the TM samples still exceeded their 3D counterparts. Strain values of the TM samples are slightly more than twice as large as the 3D samples exposed to the sulfuric acid for equal amounts of time. After exposure, larger strain values were recorded for the TM samples while decreased strain values were observed in the 3D samples. The sharp decrease in tensile stress present in the 3D samples indicates that they experienced brittle fracture. The TM samples, however, experience a much more gradual decrease in tensile stress, which is indicative of ductile fracture.

Table 1 lists the tensile stress and strain values for the traditionally manufactured samples at the different intervals of exposure time in the sulfuric acid solution. Three samples were removed after each exposure time interval and fractured using a single axial tensile test on the INSTRON. Average values for tensile stress and strain were calculated as well as their corresponding standard deviations. Standard deviations increase with exposure time, but all averages are less than one standard deviation from the adjacent corresponding averages, so these values for TM are essentially constant.

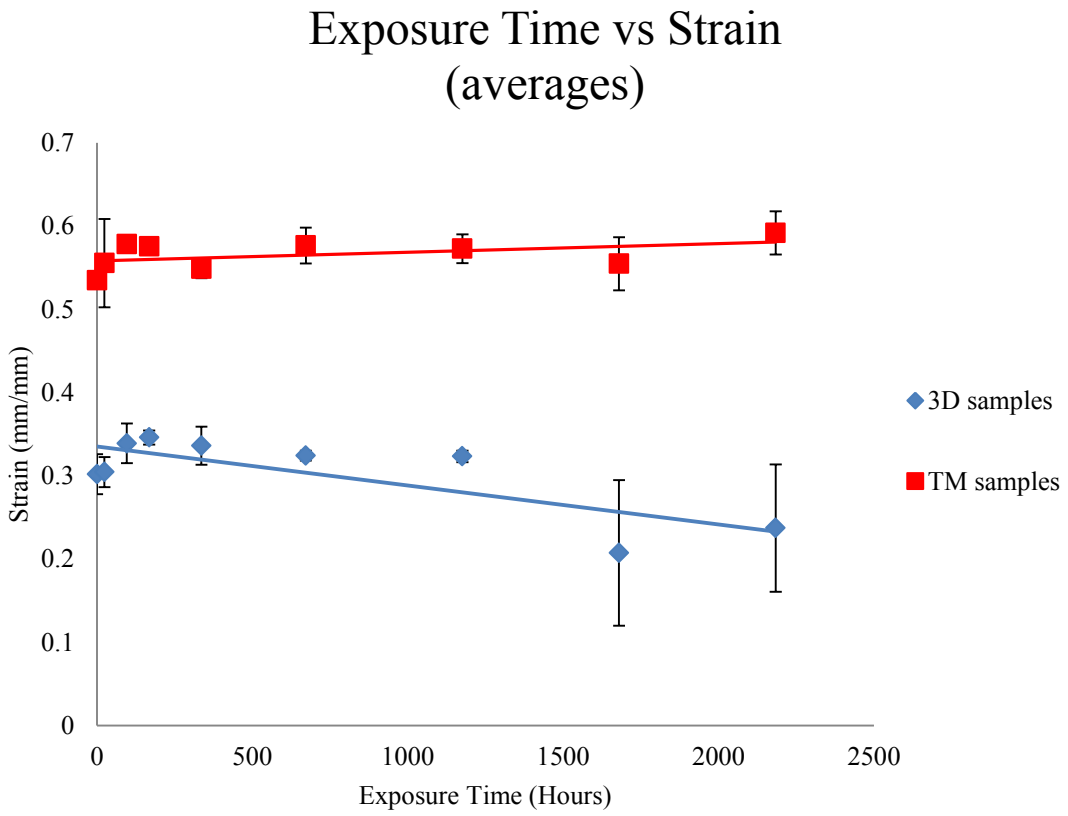

Figure 7 shows strain (in mm/mm) of both the 3D printed and traditionally manufactured samples as a function of exposure time (in hours). While a negative trend is observed between strain and exposure time with the 3D printed samples, the strain of the traditionally manufactured samples remain nearly unchanged.

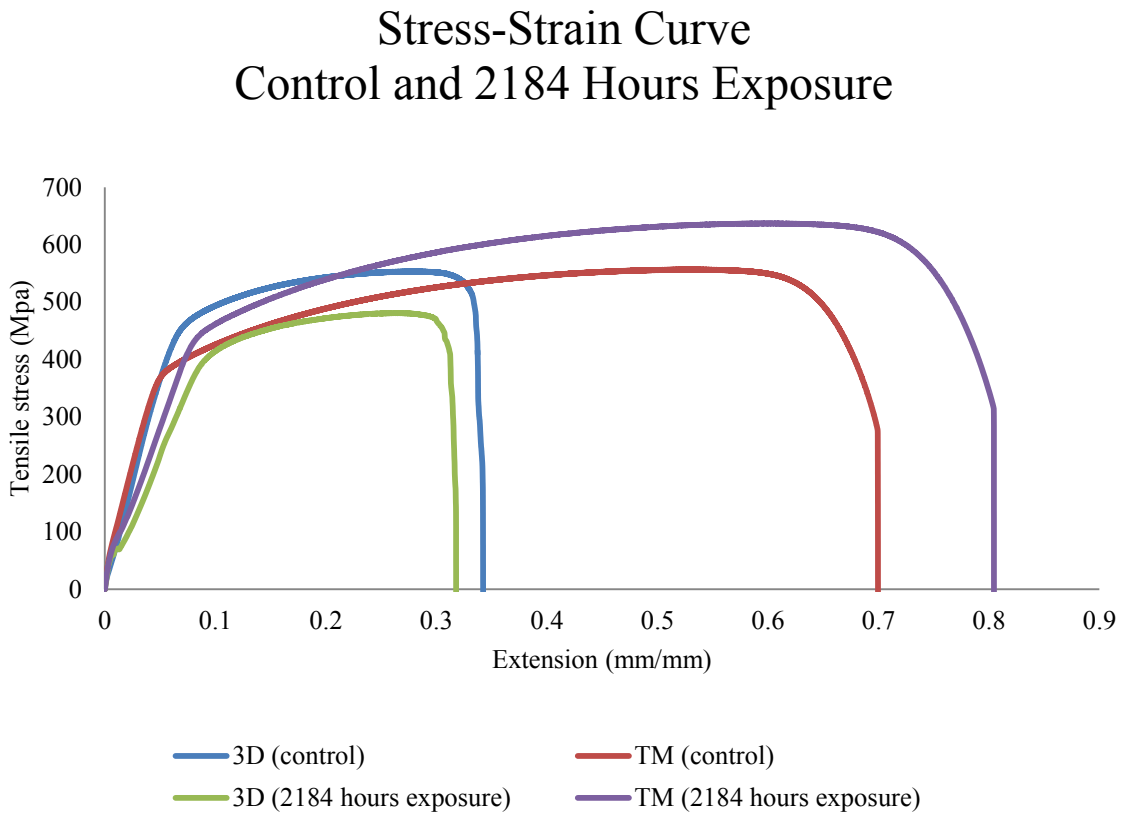

Figure 8 shows the stress-strain curve for the 3D and TM samples at 0 and 2184 hours of exposure time in the sulfuric acid solution. The TM samples demonstrated higher values of tensile stress than the 3D when comparing the control samples. After 2184 hours of exposure time, the tensile stress of the TM samples is still exceeds their 3D counterparts. Strain values of the TM samples are slightly more than twice as large as the 3D samples exposed to the sulfuric acid for equal amounts of time.

Table 1: TM Samples Compiled Data

Sample Number	Exposure time (hours)	Strain (mm/mm)	Average Strain (mm/mm)	Standard deviation	Tensile stress (MPa)	Average Tensile stress (MPa)	Standard deviation
1	0	0.542	.535	.007	562.06	574.06	25.595
2	0	0.534			603.45		
3	0	0.529			556.67		
1	24	0.591	.555	.053	521.32	542.89	33.669
2	24	0.494			525.66		
3	24	0.581			581.68		
1	96	0.573	.578	.006	572.76	572.80	13.082
2	96	0.576			585.90		
3	96	0.585			559.74		
1	168	0.581	.575	.005	563.91	569.64	8.646
2	168	0.572			579.58		
3	168	0.573			565.42		
1	336	0.557	.549	.011	589.75	596.51	8.901
2	336	0.536			593.19		
3	336	0.553			606.59		
1	672	0.594	.577	.021	601.94	590.50	20.468
2	672	0.584			602.69		
3	672	0.553			566.87		
1	1176	0.556	.573	.017	572.30	565.26	36.349
2	1176	0.572			525.90		
3	1176	0.591			597.57		
1	1680	0.528	.555	.032	565.66	562.30	35.905
2	1680	0.549			522.19		
3	1680	0.587			599.06		
1	2184	0.599	.592	.026	636.84	616.92	58.424
2	2184	0.588			610.44		
3	2184	0.588			603.49		

Table 1 lists the tensile stress and strain values for the TM samples at the different intervals of exposure time in the sulfuric acid solution. Average values and corresponding standard deviations for these measurements are also listed. Standard deviations increase with exposure time, but all averages are less than one standard deviation from the adjacent corresponding averages, so these values for TM are essentially constant.

Table 2 lists the tensile stress and strain values for the 3D printed samples at the different intervals of exposure time in the sulfuric acid solution. Three samples were removed after each exposure time interval and fractured using a single axial tensile test on the INSTRON. Average values for tensile stress and strain were calculated as well as their corresponding standard deviations. Standard deviations are nearly constant and most averages are less than one standard deviation from the adjacent corresponding averages. Increased standard deviation and decreased average values in both strain and tensile stress are easily observed after 1680 hours of exposure time. Slight differences in tensile stress and strain are observed between 336 and 672 hours as well as 1176 and 1680 hours of exposure time. This difference is minimal between 672 and 2184 hours, but a more noticeable decrease is observed in tensile stress and strain between 336 and 2184 hours of exposure time.

Figure 9 shows the SEM images taken of the samples at time 0 using the Jeol brand JSM-IT300LV before any exposure to the sulfuric acid solution. The top row shows the fracture surface of a traditionally manufactured sample at 33 (top left) and 500 (top right) times magnification. The bottom row shows the fracture surface of a 3D printed sample at the same magnifications. The traditionally manufactured sample has a much smaller fracture surface than the 3D printed sample, shown clearly in the left column. Prior to exposure to the sulfuric acid, there were no significant defects or damage to the samples.

Figure 10 shows the SEM images taken of the samples after 24 hours of exposure in the sulfuric acid solution. The top row shows the fracture surface of a traditionally manufactured sample at 33 (top left) and 500 (top right) times magnification. The bottom

Table 2: 3D Printed Samples Compiled Data

Sample Number	Exposure time (hours)	Strain (mm/mm)	Average Strain (mm/mm)	Standard deviation	Tensile stress (MPa)	Average Tensile stress (MPa)	Standard deviation
1	0	0.310	0.302	0.024	554.73	565.95	20.902
2	0	0.321			590.07		
3	0	0.275			553.06		
1	24	0.325	0.304	0.018	530.36	518.78	10.254
2	24	0.296			510.85		
3	24	0.292			515.12		
1	96	0.363	0.339	0.024	497.85	509.66	18.773
2	96	0.315			499.83		
3	96	0.339			531.31		
1	168	0.349	0.346	0.009	506.29	505.10	26.366
2	168	0.336			530.85		
3	168	0.353			478.16		
1	336	0.347	0.336	0.023	524.70	507.19	15.264
2	336	0.310			500.17		
3	336	0.352			496.69		
1	672	0.318	0.324	0.006	479.02	485.80	9.388
2	672	0.325			481.86		
3	672	0.330			496.52		
1	1176	0.328	0.323	0.007	482.06	499.96	15.756
2	1176	0.327			511.73		
3	1176	0.315			506.10		
1	1680	0.170	0.207	0.087	286.67	349.54	128.342
2	1680	0.152			335.60		
3	1680	0.300			426.36		
1	2184	0.260	0.237	0.076	480.84	471.94	73.367
2	2184	0.125			432.01		
3	2184	0.327			502.98		

Table 2 lists the tensile stress and strain values for the 3D printed samples at the different intervals of exposure time in the sulfuric acid solution. Average values and corresponding standard deviations for these measurements are also listed. Standard deviations are nearly constant and most averages are less than one standard deviation from the adjacent corresponding averages. Increased standard deviation and decreased average values in both strain and tensile stress are easily observed after 1680 hours of exposure time.

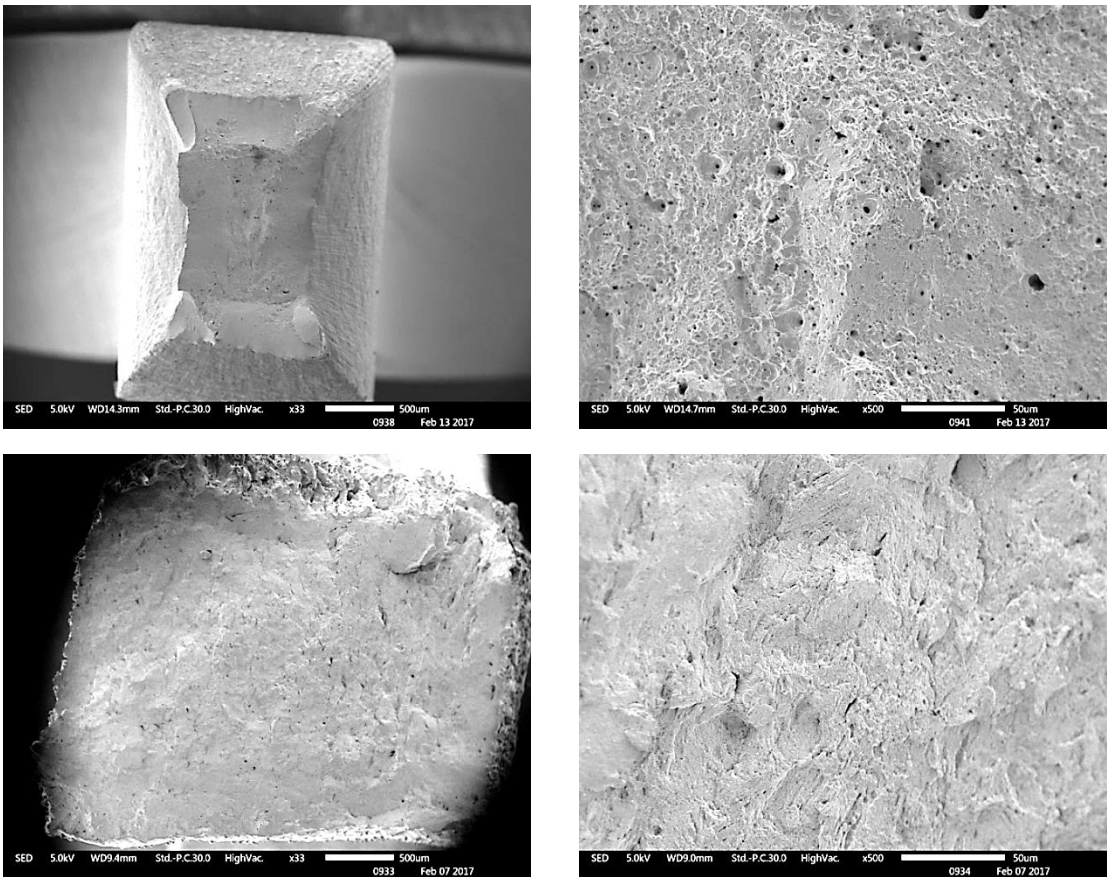

Figure 9 shows the SEM images taken of the samples at time 0 using the Jeol brand JSM-IT300LV before any exposure to the sulfuric acid solution. The top row shows the fracture surface of a traditionally manufactured sample at 33 (top left) and 500 (top right) times magnification. The bottom row shows the fracture surface of a 3D printed sample at the same magnifications. Scale bars are located in the bottom right corner of each image to accurately measure distances of the surface features. The traditionally manufactured sample has a much smaller fracture surface than the 3D printed sample, shown clearly in the left column. Prior to exposure to the sulfuric acid, there were no significant defects or damage to the samples.

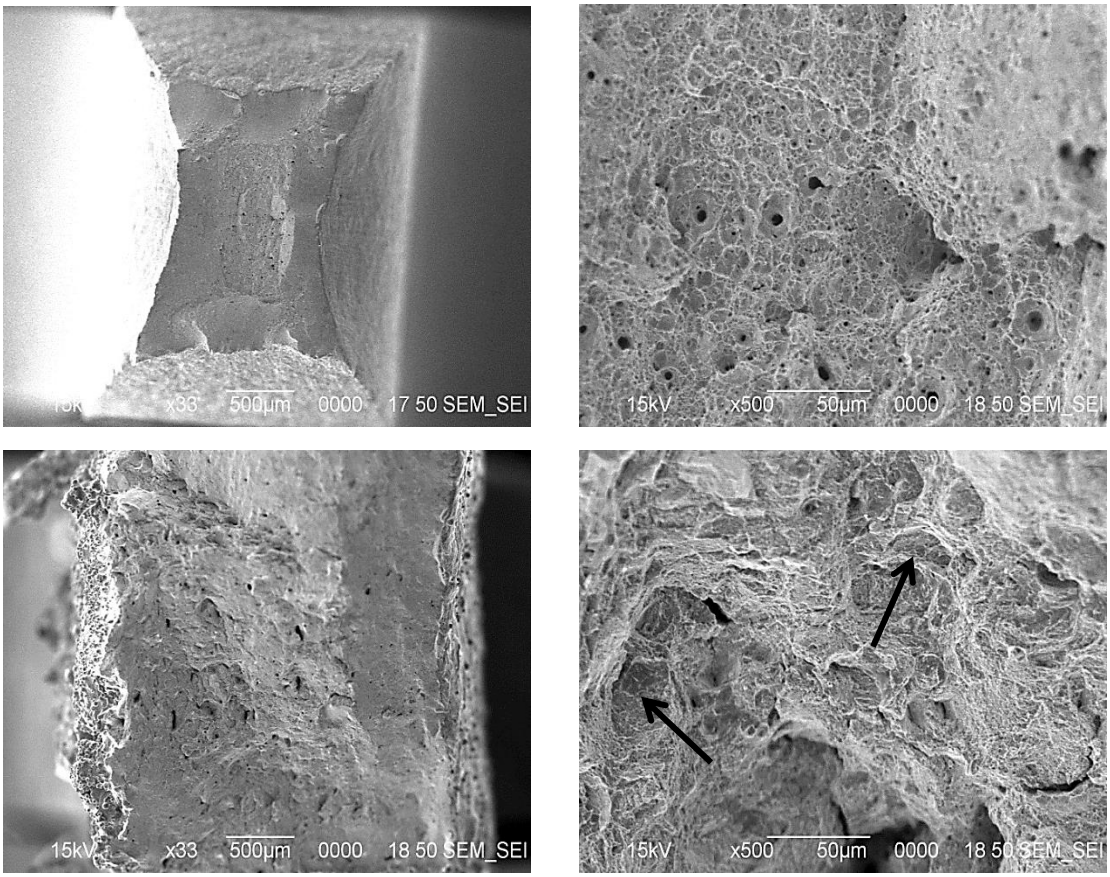

Figure 10 shows the SEM images taken of the samples using the Jeol brand JIB 4500 multi beam system after 24 hours of exposure in the sulfuric acid solution. The top row shows the fracture surface of a traditionally manufactured sample at 33 (top left) and 500 (top right) times magnification. The bottom row shows the fracture surface of a 3D printed sample at the same magnifications. The fracture surface of the traditionally manufactured sample looks nearly identical to the control images in Figure 9. However, the fracture surface of the 3D sample already shows signs of mass loss, evident by the arrows indicating the rough grooves visible in the 500 times magnification image.

row shows the fracture surface of a 3D printed sample at the same magnifications. The fracture surface of the traditionally manufactured sample looks nearly identical to the control images in Figure 9. The size of the fracture surface, as well as the size and frequency of the small holes present in the 500 times magnification image of the TM sample, show minimal changes to the corresponding image in Figure 9. However, the fracture surface of the 3D sample already shows signs of mass loss, evident by the arrows indicating the rough grooves visible in the 500 times magnification image.

Figure 11 shows the SEM images taken of the samples after 96 hours of exposure in the sulfuric acid solution. The top row shows the fracture surface of a traditionally manufactured sample at 33 (top left) and 500 (top right) times magnification. The bottom row shows the fracture surface of a 3D printed sample at the same magnifications. Differences in the fracture surface of the TM samples in Figure 11 and Figure 10 are minimal; both exhibit similar fracture surface area and small holes present on the fracture surface are of similar in shape, size, and frequency. The 3D printed sample fractured at an angle, as shown by the slope present on the surface of the 33 times magnification image. The head of the arrow present in the image points in the direction of the downward slope; focus is clearer in the top left of the image as it was closer to the focal point when the image was taken. This results in a much smoother fracture surface than in Figure 10.

Figure 12 shows the SEM images taken of the samples after 168 hours of exposure in the sulfuric acid solution system. The top row shows the fracture surface of a traditionally manufactured sample at 33 (top left) and 500 (top right) times magnification. The bottom row shows the fracture surface of a 3D printed sample at the same magnifications. Overall, the TM images compared with the corresponding images in

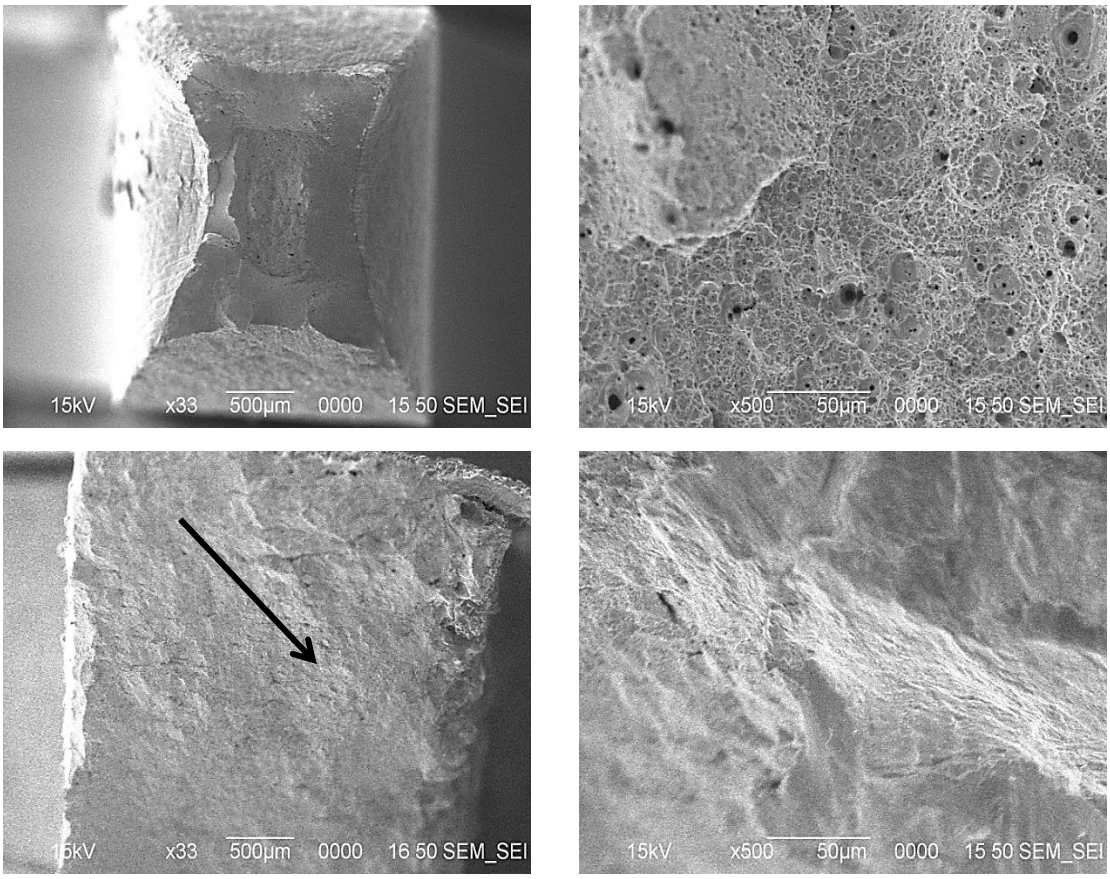

Figure 11 shows the SEM images taken of the samples using the Jeol brand JIB 4500 multi beam system after 96 hours of exposure in the sulfuric acid solution. The top row shows the fracture surface of a traditionally manufactured sample at 33 (top left) and 500 (top right) times magnification. The bottom row shows the fracture surface of a 3D printed sample at the same magnifications. Differences in the fracture surface of the TM samples in Figure 11 and Figure 10 are minimal; both exhibit similar fracture surface area and small holes present on the fracture surface are of similar in shape, size, and frequency. The 3D printed sample fractured at an angle, as the slope present on the surface of the 33 times magnification image shows. This results in a much smoother fracture surface than in Figure 10.

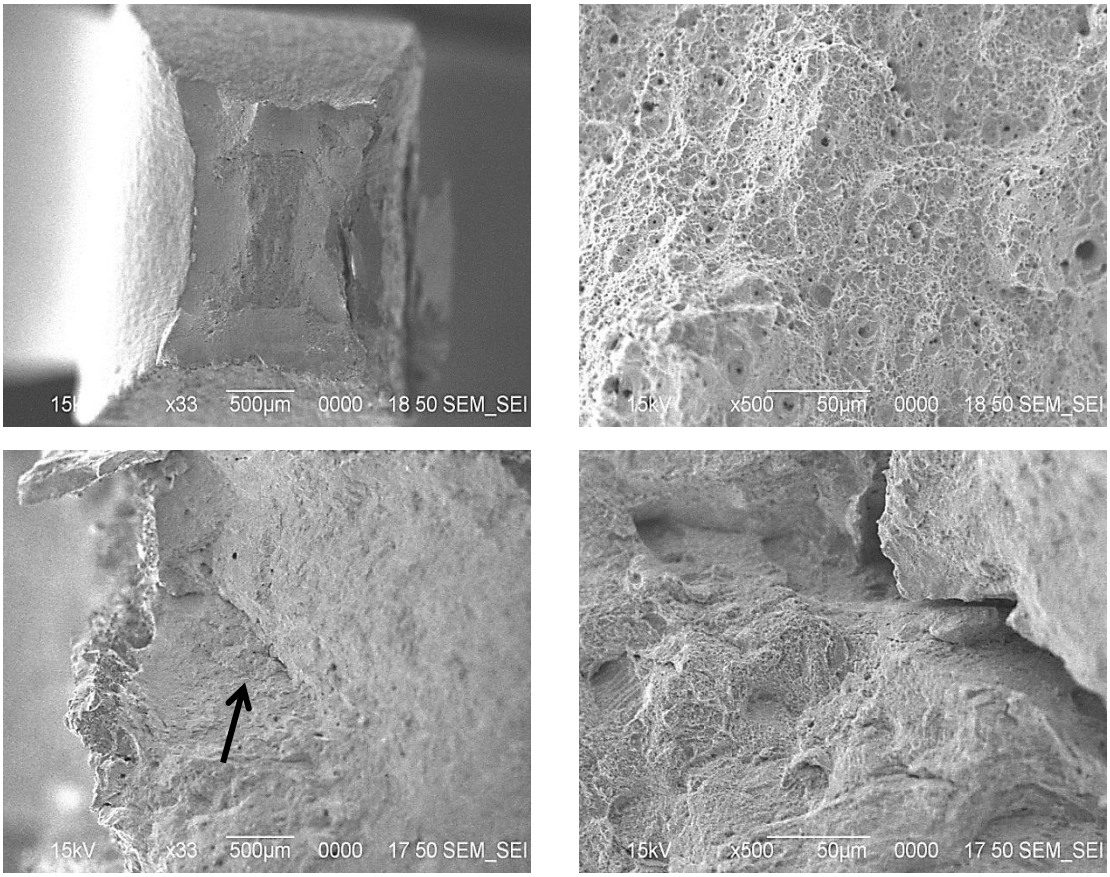

Figure 12 shows the SEM images taken of the samples using the Jeol brand JIB 4500 multi beam system after 168 hours of exposure in the sulfuric acid solution system. The top row shows the fracture surface of a traditionally manufactured sample at 33 (top left) and 500 (top right) times magnification. The bottom row shows the fracture surface of a 3D printed sample at the same magnifications. Overall, the TM images compared with the corresponding images in Figure 11 show very few differences. The fracture surfaces are nearly identical in size, and the features of the surfaces show minimal differences in shape, size, or number of small holes present. The images taken of the 3D printed sample are slightly off-center because the fracture occurred at a very steep angle; therefore, the focal point of the image became the smoothest section of the fracture surface indicated by the arrow in the 33 times magnification image.

Figure 11 show very few differences. The fracture surfaces are nearly identical in size, and the features of the surfaces show minimal differences in shape, size, or number of small holes present. The images taken of the 3D printed sample are slightly off-center because the fracture occurred at a very steep angle; therefore, the focal point of the image became the smoothest section of the fracture surface indicated by the arrow in the 33 times magnification image. A crack can be seen in the 500 times magnification image of the 3D sample fracture surface, indicating that corrosion occurred and weakened the sample from within.

Figure 13 shows the SEM images taken of the samples after 336 hours of exposure in the sulfuric acid solution. The top row shows the fracture surface of a traditionally manufactured sample at 33 (top left) and 500 (top right) times magnification. The bottom row shows the fracture surface of a 3D printed sample at the same magnifications. The focal point of the image of the 3D sample is the smoothest section of the fracture surface indicated by the arrow in the 33 times magnification image. The TM sample images in Figure 13 were similar to the TM control images in Figure 9; the surface area of the fracture surface, as well as the number and size of the small holes on the fracture surface, are nearly identical. The 3D printed sample shows signs of lost mass from the visible holes in the 500 times magnification image indicated by the arrows present.

Figure 14 shows the SEM images taken of the samples after 672 hours of exposure in the sulfuric acid solution. The top row shows the fracture surface of a traditionally manufactured sample at 33 (top left) and 500 (top right) times magnification. The bottom row shows the fracture surface of a 3D printed sample at the same

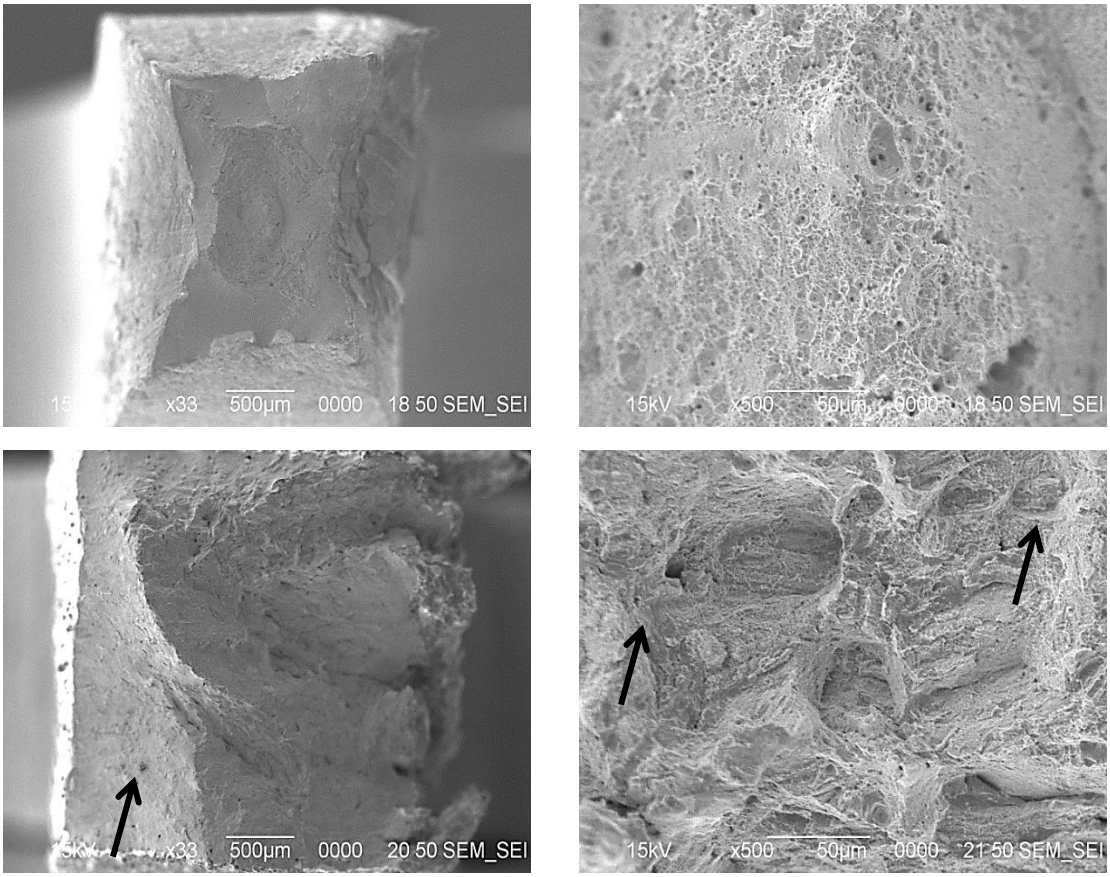

Figure 13 shows the SEM images taken of the samples using the Jeol brand JIB 4500 multi beam system after 336 hours of exposure in the sulfuric acid solution. The top row shows the fracture surface of a traditionally manufactured sample at 33 (top left) and 500 (top right) times magnification. The bottom row shows the fracture surface of a 3D printed sample at the same magnifications. The TM sample images in Figure 13 were similar to the TM control images in Figure 9; the surface area of the fracture surface as well as the number and size of the small holes on the fracture surface are nearly identical. The focal point of the 3D image is the smoothest section of the fracture surface indicated by the arrow in the 33 times magnification image. The 3D printed sample shows signs of lost mass from the visible holes in the 500 times magnification image indicated by the arrows present.

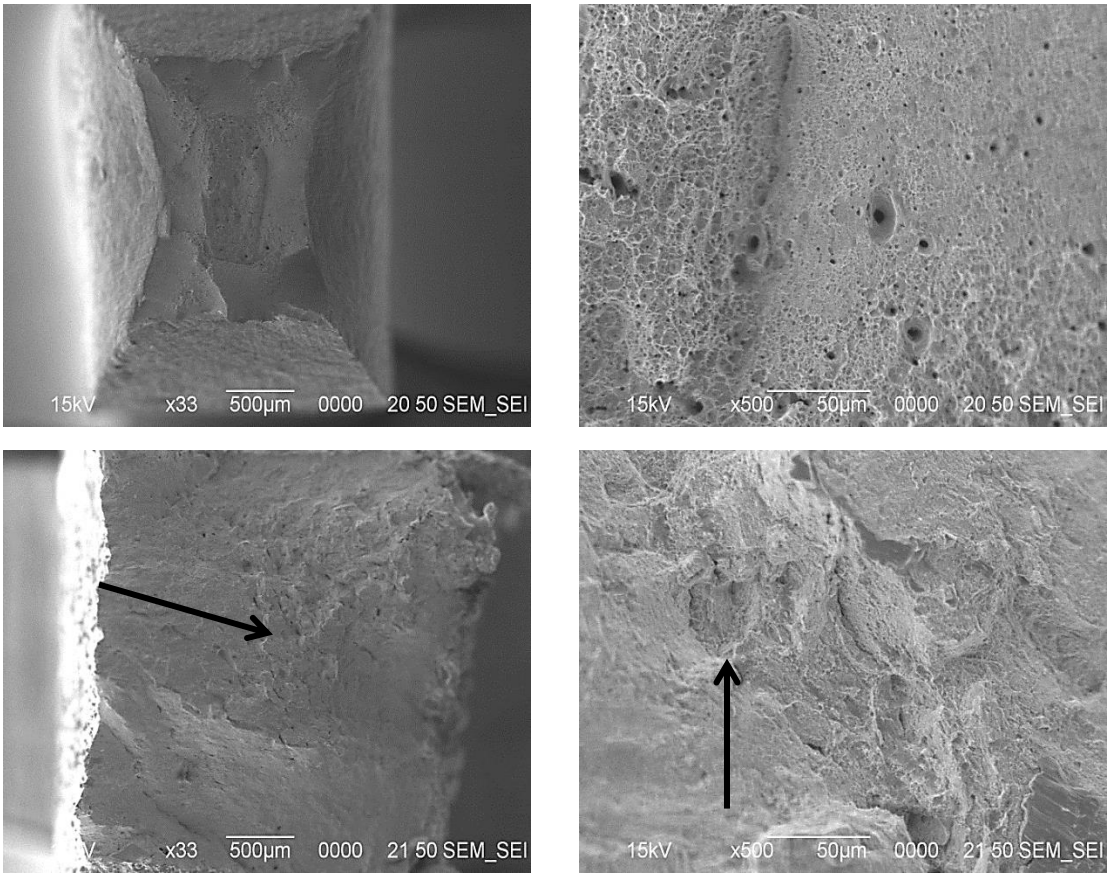

Figure 14 shows the SEM images taken of the samples using the Jeol brand JIB 4500 multi beam system after 672 hours of exposure in the sulfuric acid solution. The top row shows the fracture surface of a traditionally manufactured sample at 33 (top left) and 500 (top right) times magnification. The bottom row shows the fracture surface of a 3D printed sample at the same magnifications. The fracture surface of the traditionally manufactured sample in Figure 14 was still nearly identical to the TM control images in Figure 9. The fracture surface of the 3D sample shows minimal signs of mass loss; the grooves indicating lost mass are less prominent due to the slope of the fracture surface. The arrow in the 33 times magnification image of the 3D sample indicates the direction of the slope with the lowest point on the fracture surface near the head of the arrow.

magnifications. The fracture surface of the traditionally manufactured sample in Figure 14 was still nearly identical to the TM control images in Figure 9, as shown by the predominately smooth fracture surfaces as well as the consistent fracture surface areas. The fracture surface of the 3D sample shows minimal signs of mass loss, although some indentation is present, as noted by the arrow; the grooves indicating lost mass are less prominent due to the slope of the fracture surface. The arrow in the 33 times magnification image of the 3D sample indicates the direction of the slope with the lowest point on the fracture surface near the head of the arrow.

Figure 15 shows the SEM images taken of the samples after 1176 hours of exposure in the sulfuric acid solution. The top row shows the fracture surface of a traditionally manufactured sample at 33 (top left) and 500 (top right) times magnification. The bottom row shows the fracture surface of a 3D printed sample at the same magnifications. The traditionally manufactured sample has a much smaller fracture surface than the 3D printed sample, shown clearly in the left column. The size and frequency of the small holes in the traditionally manufactured sample have increased compared to the control images in Figure 9. Larger holes are present in the 3D printed samples as indicated by the arrows in the 33 times magnification image.

Figure 16 shows the SEM images taken of the samples after 1680 hours of exposure in the sulfuric acid solution. The top row shows the fracture surface of a traditionally manufactured sample at 33 (top left) and 500 (top right) times magnification. The bottom row shows the fracture surface of a 3D printed sample at the same magnifications. The images of the traditionally manufactured sample are very similar to those in Figure 15, as shown by the relatively smooth fracture surfaces as well as the

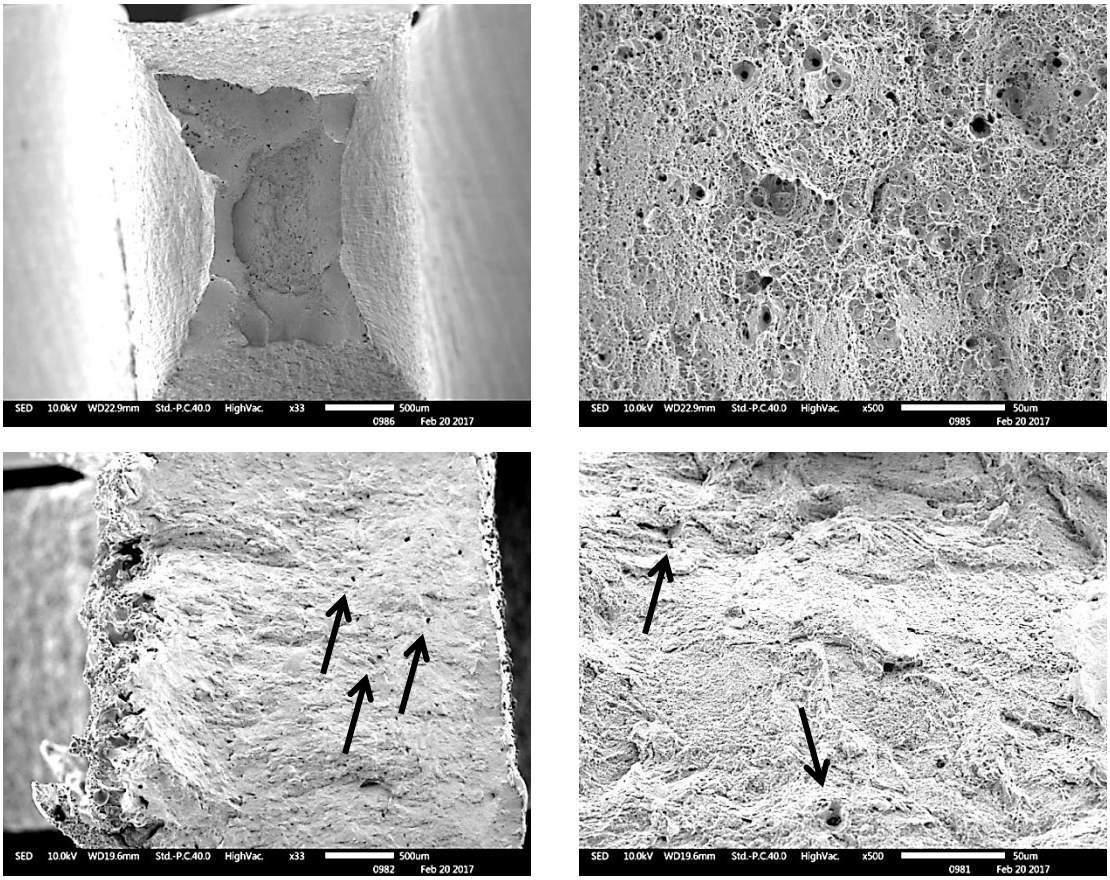

Figure 15 shows the SEM images taken of the samples using the Jeol brand JSM-IT300LV after 1176 hours of exposure in the sulfuric acid solution. The top row shows the fracture surface of a traditionally manufactured sample at 33 (top left) and 500 (top right) times magnification. The bottom row shows the fracture surface of a 3D printed sample at the same magnifications. The traditionally manufactured sample has a much smaller fracture surface than the 3D printed sample, shown clearly in the left column. The size and frequency of the small holes in the traditionally manufactured sample have increased compared to the control images in Figure 9. Larger holes are present in the 3D printed samples as indicated by the arrows in the 33 times and 500 times magnification images.

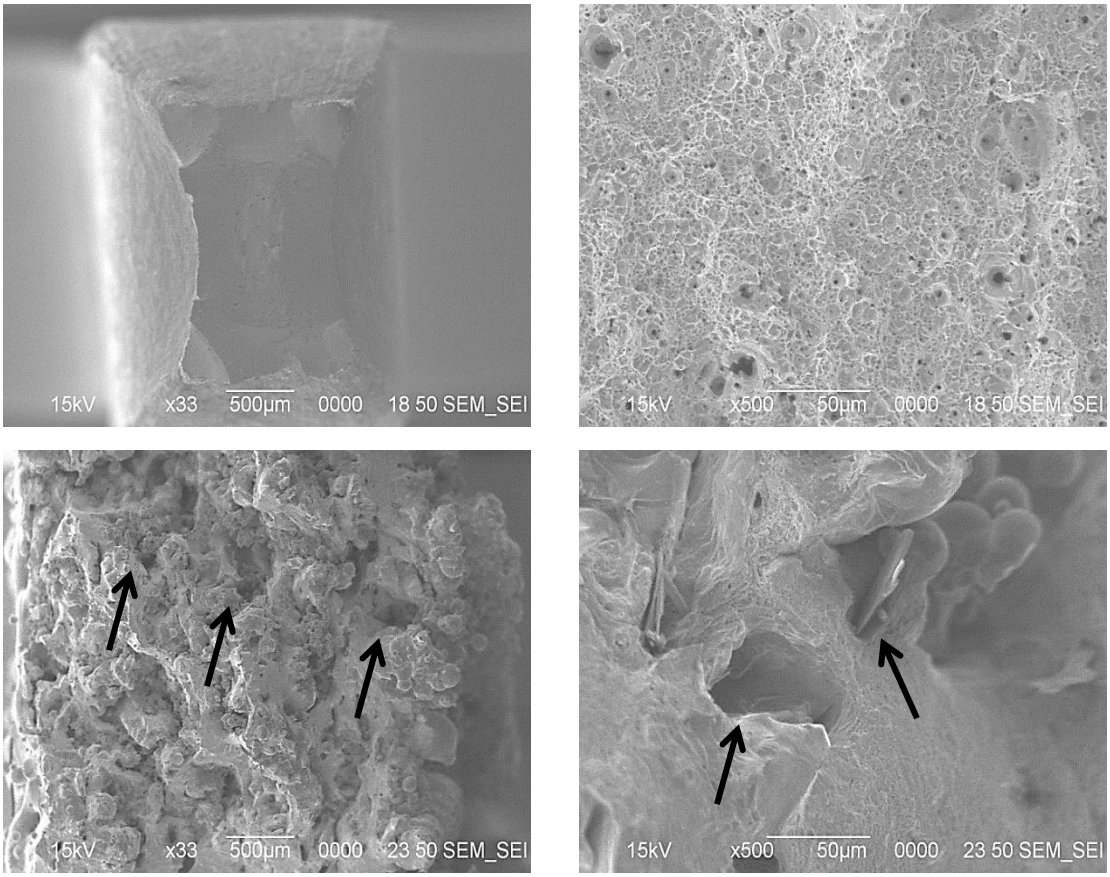

Figure 16 shows the SEM images taken of the samples using the Jeol brand JIB 4500 multi beam system after 1680 hours of exposure in the sulfuric acid solution. The top row shows the fracture surface of a traditionally manufactured sample at 33 (top left) and 500 (top right) times magnification. The bottom row shows the fracture surface of a 3D printed sample at the same magnifications. The images of the traditionally manufactured sample are very similar to those in Figure 15. The 3D printed images show dramatic signs of corrosion and mass loss, which is evident by the jagged fracture surface and large holes indicated by the arrows on both the 33 and 500 times magnification images.

consistent fracture surface areas. The 3D printed images show dramatic signs of corrosion and mass loss, which is evident by the jagged fracture surface and large holes indicated by the arrows on both the 33 and 500 times magnification images.

Figure 17 shows the SEM images taken of the samples after 2184 hours of exposure in the sulfuric acid solution. The top row shows the fracture surface of a traditionally manufactured sample at 33 (top left) and 500 (top right) times magnification. The bottom row shows the fracture surface of a 3D printed sample at the same magnifications. The traditionally manufactured sample has a much smaller fracture surface than the 3D printed sample, shown clearly in the left column. The size and frequency of the small holes in the traditionally manufactured sample increased slightly compared to Figure 16. The 3D printed sample has corroded even more than the 3D sample in Figure 16. The holes in this sample are more pronounced and are indicated with arrows for clarity.

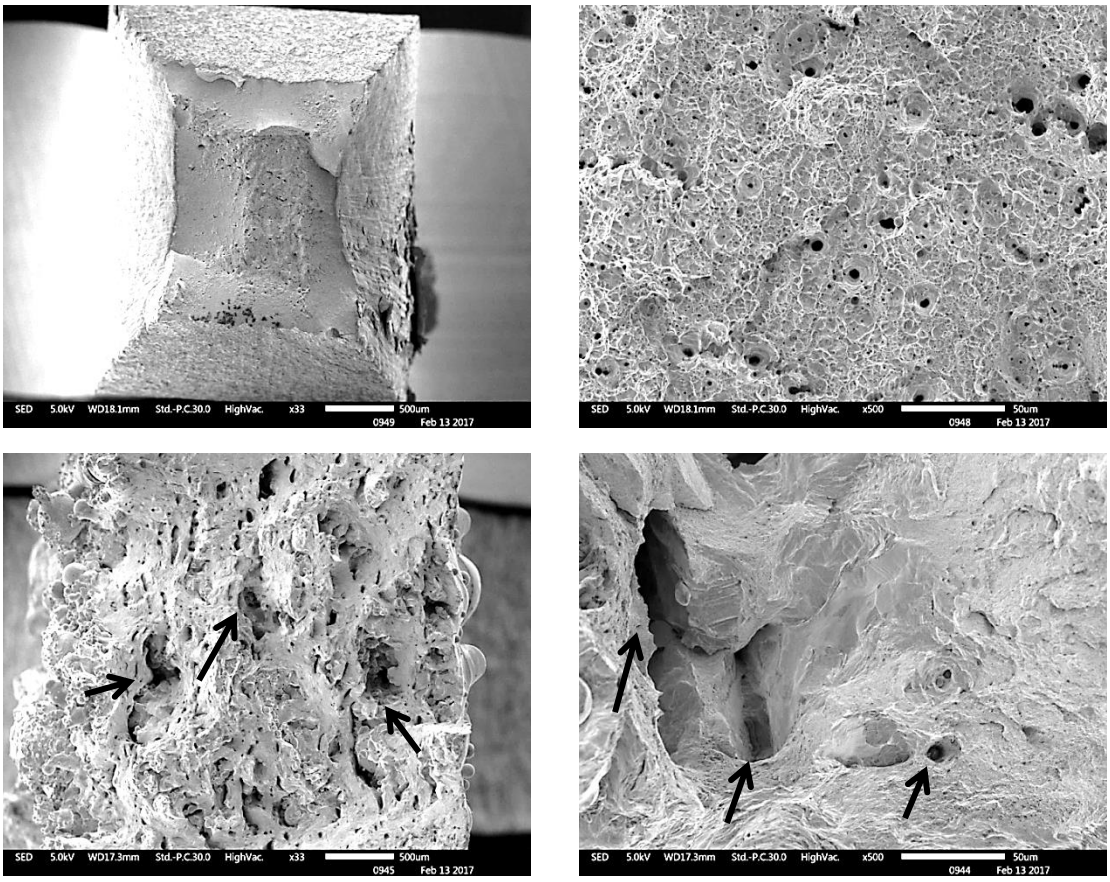

Figure 17 shows the SEM images taken of the samples using the Jeol brand JSM-IT300LV after 2184 hours of exposure in the sulfuric acid solution. The top row shows the fracture surface of a traditionally manufactured sample at 33 (top left) and 500 (top right) times magnification. The bottom row shows the fracture surface of a 3D printed sample at the same magnifications. The traditionally manufactured sample has a much smaller fracture surface than the 3D printed sample, shown clearly in the left column. The size and frequency of the small holes in the traditionally manufactured sample increased slightly compared to Figure 16. The 3D printed sample has corroded even more than the 3D sample in Figure 16. The holes in this sample are more pronounced and are indicated with arrows for clarity.

4.0 Discussion

The amount of time chosen to expose the different sample types to the sulfuric acid solution was set for 2184 hours. As the standard amount of exposure time for a corrosion study is only 1000 hours and stainless steel is inherently resistant to corrosion due to the alloying elements present, this limited amount of time may not have allowed the effects of the corrosive environment to be easily observed. Therefore, the standard amount of exposure time was more than doubled to ensure the mechanisms of corrosion taking place would cause enough damage to characterize them.

Figure 2 shows micrographs of the samples before exposure in the sulfuric acid solution with the traditionally manufactured (TM) samples on the top row and the 3D printed (3D) samples on the bottom row. At time 0, there are no distinct differences between the surfaces of the samples other than those caused by the method of production. The visibly rough surface on the 3D samples is caused by the Laser Powder Bed Fusion (LPBF) process, while the characteristic lines and smoother finish of the TM samples are caused by the rolling process used to produce standard sheet metal.

Figure 3 shows the same samples in Figure 2 (TM samples on the top row and the 3D samples on the bottom row) after 2184 hours of exposure time in the sulfuric acid solution. The 3D samples show more signs of damage than their TM counterparts. The arrows present in Figure 3 indicate areas where mass has been removed from the 3D sample. Small and numerous holes on the 3D sample show where the surface of the sample was attacked by the corrosive ions. This contrasts with the TM samples, which show no clear signs of mass loss after 2184 hours of exposure. Almost no differences are observed when comparing the TM samples in Figures 2 and 3. However, the surfaces of

the 3D samples in Figure 3 are much rougher and more damaged than those in Figure 2. Comparing Figures 2 and 3, the sulfuric acid corroded the 3D samples much more than the TM samples.

The observations made in Figures 2 and 3 are confirmed when the mass loss of the two sample types are compared. Figure 4 compares the cumulative mass lost over the 2184 hours of exposure time between the 3D and TM samples. The TM samples lost a total of only 0.004g while the 3D samples lost 0.014g, meaning the rate of mass loss was more than three times higher in the 3D samples.

Figure 5 compares the density of the TM and 3D samples over the 2184 hours of exposure time. Because the LPBF process melts the metal powder used in creating the 3D samples in very thin individual layers, voids are left in between each of these layers as they are unable to arrange into their lowest energy conformation, which in turn would decrease the initial density of the 3D samples. The particles can only reach their lowest energy conformation when given enough time for all of the available particles to interact with one another, as well as a slow cooling rate, which is characteristic of the TM production method. The density of the TM samples remained relatively constant even as the exposure time increased from 0 to 2184 hours. The characteristically smooth surface of the TM samples observed in Figures 2 and 3 forced the corrosive ions to only attack the surface; therefore, the TM samples did not experience significant mass loss or surface damage.

The density of the 3D samples also stayed constant as the exposure time increased from 0 to 2184 hours. However, Figure 4 shows that these samples lost more than three times as much mass as the TM samples. If the density of these samples did not change, it

is likely the mass lost was from the surface of the 3D samples. The rough surface of the 3D samples observed in Figures 2 and 3 allowed for the corrosive ions to more easily penetrate the sample and remove mass from the surface.

The error bars in Figure 5 are large compared to the axis of the figure, but the size of the error bars can be attributed to the variation in volume of the individual samples. Little variation was observed in the mass of the samples; however, the dimensions of the samples were not initially identical, and this variation impacted the average values of density. Average values for mass and volume were calculated from the three samples of each production method exposed for a given amount of time in the sulfuric acid solution. The standard deviation for each group of samples, therefore, was large compared to their relatively constant values of density. So, even though the error bars for this data is large, it was concluded that the density for both the 3D and TM samples remained essentially constant as the exposure time in the sulfuric acid solution increased.

Figures 6 and 7 illustrate the tensile stress and the strain which the 3D and TM samples could withstand upon fracture in a single axial tensile test. At time 0, the TM samples exhibited higher tensile stress (575MPa) and strain (0.55mm/mm) values than the 3D samples (500MPa and 0.3mm/mm, respectively). Figure 6 shows that the tensile stress of the TM samples is not influenced by exposure time. The corrosive ions are able to slightly damage the surface of these samples, but they are unable to penetrate the surface to cause further damage. Limiting the damage to the surface of the samples allows for the tensile stress of the TM samples to remain constant. In order for a change in the tensile stress to occur, either the mass or the surface area of the samples would need to change. However, Figure 2-4 shows minimal mass loss and surface damage to the

TM samples. Therefore, the tensile stress and elongation for the TM samples are not affected by the increased exposure time.

Conversely, as seen in Figures 6 and 7, the 3D samples experienced noticeable decreases to both tensile stress and strain. Both stress and strain decrease slowly from time 0 to 1176 hours of exposure time, and then drastically after 1176 hours. Tensile stress of the 3D samples decreased by roughly 15% from the control values, and the strain values of these samples decreased by about 25% after 2184 hours of exposure time. Initially, the 3D samples were hypothesized to have a lower density than the TM samples, which would allow for the samples to be more easily penetrated by the corrosive ions and cause mass loss from both the surface and within the samples themselves. However, Figure 5 shows the density of samples using both production methods were constant and very similar to each other. In order for the mechanical properties of the samples to be impacted, the mass lost from the samples would have to be substantial enough to cause a change in surface area. This is contradicted by Figure 4, which shows that the samples lost very small amounts of mass relative to the total mass of the samples. The corrosive environment did not cause the samples to lose enough mass to impact their mechanical properties, yet the 3D samples still saw a decrease in both tensile stress and strain.

Originally, it was hypothesized that the porosity of the 3D samples would be greater than the porosity of the TM samples and that the difference in production method would cause the 3D samples to be less dense than their TM counterparts. Additionally, the 3D samples were assumed to have a rougher surface area than the TM samples, which would potentially allow the corrosive ions to more easily penetrate the 3D samples. Due to this assumed density difference, as well as the notably rougher surface present of the

3D samples, it was also hypothesized that the 3D samples would lose significantly more mass than the TM samples. However, the amount of mass lost from both sample types was very small compared to the overall mass of the samples. Mass loss of the 3D samples was approximately 0.1% of the total sample mass while TM samples lost 0.04% of the sample mass. Because the density of the samples both remained constant during the time they were exposed to the sulfuric acid solution (Figure 5), it was concluded that the mass lost from these samples was from the surface.

Without significant mass loss or differences in density observed comparing the 3D with the TM samples, another mechanism must be responsible for the decreases in tensile stress and strain in the 3D samples. Hydrogen embrittlement is the most likely mechanism to cause the differences in the fracture surfaces, as well as the resulting decreases in mechanical properties of the 3D samples compared to their TM counterparts. Increased surface roughness of the 3D samples allowed for the corrosive ions to penetrate and react chemically with the material in the 3D samples. The reactions formed brittle solid compounds within the bulk of the samples, causing the mechanical properties to change. These brittle compounds would not change the density or impact the amount of mass lost within the samples, supported by Figures 5 and 4, respectively. Only the chemical bonds of the affected areas of the sample would be altered, but these changes would impact the mechanical properties of the 3D samples (Figures 6 and 7).

In Figures 6 and 7, a large drop is observed between 1176 and 1680 hours for the 3D samples. One possible explanation for this would be from variation inherent in the LPBF process used to produce the 3D samples. As the powder is laid across the stage and selectively melted, variances in spreading the powder across the stage could lead to

inconsistencies in the sample produced. Variation in the composition of the powder itself could also cause fluctuations in the mechanical properties of the samples. However, if this were the case, there would reasonably be more than only one sample affected. The most likely reason for the inconsistent data comes from the loading of the samples when executing the tensile test. Manual grips are operated by the user to hold the sample in place, and a small amount of torque can be inadvertently applied to the sample if loaded improperly. Applied torque would cause the sample to fail at a lower tensile stress than the trend suggests and account for the large standard deviation in the data. This would also explain why the samples after 2184 hours of exposure time had higher tensile stress and strain values than the samples after only 1680 hours of exposure time; proper loading of the samples resulted in a more linear trend, which follows the other data points more closely.

As seen in the cumulative stress strain curve (Figure 8), the 3D samples experienced a sharp decrease in tensile stress just before fracture occurred during tensile testing. The sudden failure of the samples under these conditions is characteristic of brittle fracture. This supports the assertion that the 3D samples contain additional residual stress; necking cannot take place within the 3D samples because the molecules are unable to stretch to alleviate the stress. Therefore, the only way for the 3D samples to relieve the stress is to fracture. The TM samples, however, experienced a more gradual decrease in tensile stress. This, along with the reduction in fracture surface area observed in the TM samples, indicates that they experienced ductile fracture.

The maximum tensile stress and strain of the TM samples remained nearly unchanged after 2184 hours of exposure in the sulfuric acid solution, while decreases in

both tensile stress and strain values were observed in the 3D samples compared to their respective control samples. This supports the theory that hydrogen embrittlement is the mechanism responsible for the corrosion taking place within the samples. As the solution reacted chemically with the samples, brittle precipitates were formed within the samples. The 3D samples were more easily penetrated by the sulfuric acid, allowing more precipitates to form within these samples and, in turn, changing the mechanical properties of the 3D samples. Increased amounts of these brittle precipitates decreased the ductility of the sample and hindered its ability to resist fracture. This, in turn, explains the decreases in tensile stress and strain in the 3D samples after prolonged exposure to the sulfuric acid solution.

Figure 8 shows the TM sample after 2184 hours of exposure time having slightly higher tensile stress and strain values than the control sample; however, this difference is within the standard deviations calculated for these values in Table 1. The increase in both tensile stress and strain fall within the standard deviations calculated. Therefore, the observed increase can be attributed to normal variation between samples. Increased exposure time in the corrosive environment did not increase the tensile stress or strain of the TM samples.

Table 2 shows variation in the average values of tensile stress and strain for the 3D printed samples as well as their respective standard deviations. The deviation after 1680 hours of exposure is much larger than the other intervals of exposure time. This is likely due to unintended additional torque applied to the sample during tensile testing, as described previously concerning Figure 7. The average values of both tensile stress and strain decreased after 1680 hours of exposure for the 3D samples, unlike the TM samples.

The decreases in tensile stress and strain values observed in Table 2 are supported by Figures 6 and 7, which show decreasing linear trends for both of these properties as a function of exposure time for the 3D samples. This decrease in mechanical properties for the 3D samples supports that these samples experienced more damage through hydrogen embrittlement than their TM counterparts.

Figure 9 shows the scanning electron microscope (SEM) images of the fracture surfaces of the TM samples in the top row and the 3D samples in the bottom row at low and high magnifications. Before any exposure to the sulfuric acid solution, there are very clear differences between the fracture surfaces of the 3D and TM samples. Comparing the low magnification images of the TM and 3D samples in Figure 9, the surface area of the fracture surface is much larger on the 3D sample than the TM. The area of the 3D sample shows minimal changes from the original dimensions of the samples as described in Figure 1; however, a clear reduction in area is observed for the TM sample. As the TM samples were pulled apart in the tensile test, they experienced plastic deformation from necking. Evidence of necking is observed by the gradual decrease in tensile stress as the TM samples approach their maximum extension before fracture (Figure 8). The manner in which the TM samples were produced allowed them to withstand more stress and strain because the molecules of the metal were given enough time to settle into the lowest possible energy state. When the TM samples were first put under stress, the bonds of the molecules were able to stretch out and the samples only deformed elastically. In order to see plastic deformation occur, more energy was required to break the bonds that were previously only stretched. As the load on the sample increased, the TM samples attempted to prevent failing by reducing the surface area through necking. If the same

load is applied to a smaller surface area, the sample will stretch out and deform plastically before fracturing completely. Once the sample can no longer deform plastically in this way, the sample will experience ductile fracture. Figure 9 shows this clearly, as the surface area of the TM fracture surface is much smaller than the original dimensions described in Figure 1.

On the other hand, the 3D samples did not show any reduction in area upon fracturing in the tensile test. During production, the molecules of the 3D samples did not have time to settle into the lowest energy confirmation the same way as the TM samples. Instead of all of the molten metal cooling together at a constant rate, the 3D samples solidified in layers that were independent of one another. In the LPBF process, each thin layer of powder is heated rapidly when contacted by the laser. The molten powder only remains in the liquid phase for a short time before solidifying, and it can only interact with the thin solid layer of material beneath it. This holds true for each subsequent layer of powder, resulting in minimal interaction of the powder within the 3D samples. Reduced interaction of molecules and faster cooling times also encourage the formation of potential slip planes within the 3D samples. Without the chance to interact and settle into a lower energy conformation, residual stress can build up within the sample. Confirmation of this residual stress is found with the lower stress and strain values in Figures 6 and 7. Additionally, Figure 8 shows a rapid decrease in tensile stress for the 3D samples as they approach their maximum values of strain. The residual stress, low strain value, sharp decrease in tensile stress, and larger fracture surface all assert that the 3D samples experienced brittle fracture, unlike the TM samples.

It should be noted that TM samples experienced an increase in both strain and tensile stress after exposure to the sulfuric acid solution when looking at the stress-strain curve, which does not follow the trend described previously with the 3D samples or the graphs in Figures 6 and 7. One possible explanation for this unexpected trend comes from the selection of the samples used in the study. The largest samples of each type were designated to be the samples that would be exposed to the sulfuric acid solution the longest. The TM samples, however, did not experience the same amount of negatively impacted mechanical properties as the 3D samples did. Therefore, the fact that the larger samples were used in the later part of the study could account for the increase in tensile stress. The larger TM samples have nearly identical surface areas to the control samples, but they also have more mass. Because the effects of the sulfuric acid solution were minimal, the larger TM samples are shown to have higher tensile stress values. This trend was followed for the 3D samples as well; however, the corrosive environment impacted the 3D samples much more than the TM samples. The strain of the 3D samples exposed for 2814 hours is slightly less than the control samples, 0.32mm/mm and 0.35mm/mm, respectively. On the other hand, the maximum tensile stress of the exposed samples (480MPa) is much less than the control samples (550MPa) as seen in Figure 8. Therefore, the potentially larger 3D samples used at the end of the study were not stronger than the control samples after they had been exposed.

In addition to the surface area of the fracture surface, the physical features of the fracture surface also differ between the TM and 3D samples at time 0. Small holes are present in the fracture surface of the TM samples, as shown in the 500 times magnification image of Figure 9 (top right). However, these holes are not visible in the

3D samples at the same magnification (bottom right). As the samples have not yet been exposed to the sulfuric acid solution, the cause for this difference is likely based on the method used to produce the samples. The TM samples, which experienced ductile fracture, took longer to fail than the 3D samples. This extended time allowed for the grains and molecules to stretch before failure. Once the sample finally failed, some of the particles that were held within the portion of the gage length where failure occurred were removed mechanically. On the 3D samples, however, the failure of the 3D samples, which experienced brittle fracture, occurred much more quickly. The samples did not have time to stretch out and, instead, fractured along a slip plane within the structure of the samples. When fracture occurs on the slip plane, a cleaner break is produced, resulting in a smoother fracture surface.

Figures 10 through 15 show the fracture surfaces of the samples at the same magnifications as Figure 9 after varying lengths of exposure time in the sulfuric acid solution. Comparing the images of the TM samples in each of the figures, minimal differences are observed. The areas of the fracture surface in each of the images are similar to that of the TM sample at time 0. The TM samples in these figures all fractured after necking with the surface of the fracture perpendicular to the force applied in the tensile test. Small holes are present in the 500 times magnification of the TM samples in all of these figures, but the frequency of these holes are relatively constant between images. Similarly, the surface area of the fracture surfaces and the frequency of the small holes present on the 3D samples show little change between Figures 10 and 15.

However, there is more variation in the 3D samples than in the TM samples regarding the fracture surface characteristics. The 3D images in Figure 10 already

showed signs of damage from the sulfuric acid. Compared to the control 3D images in Figure 9, there are visible differences on the fracture surface, as indicated by the arrows in Figure 10. These indentations show where pieces of the sample have been removed, which were most likely induced by hydrogen embrittlement within the sample as discussed previously. The brittle precipitates that form as a result of the chemical reaction between the metal and the corrosive ions produce localized areas of the sample that are more brittle than the bulk material. Upon tensile testing, these areas are broken off from the sample, leaving the indentations on the fracture surface.

The 3D images in Figure 11, although they were exposed to the sulfuric acid longer than the samples in Figure 10, have less holes and indentations on the fracture surface. However, the sloped fracture surface indicated by the arrow in the 33 times magnification image for the 3D sample in Figure 11 demonstrates that damage still occurred. The fracture surface of a sample subjected to a uniaxial tensile test should be perpendicular to the direction of the force applied during the test. The angled fracture surface observed in Figure 11 indicates that a slip plane was present along which the sample was more easily fractured. This slip plane was not present in the same location on the 3D samples in Figures 9 or 10, and increased exposure time had a negative impact on the mechanical properties of the 3D samples (Figures 6 and 7). The slip plane was mainly activated because the corrosive ions penetrated the 3D sample enough to weaken the bulk of the sample by forming brittle precipitates throughout. With enough localized areas becoming more brittle, a slip plane was weakened so that the sample fractured along it, accounting for the smooth but angled fracture surface.

Further evidence of this explanation is observed in the 3D images of Figure 12. Similar to the 3D images in Figure 11, the fracture surface is smooth and angled; however, the fracture surface in Figure 12 follows multiple slip planes instead of a single slip plane as in Figure 11. The arrow in Figure 12 indicates where some of the slip planes meet. As this sample was exposed to the sulfuric acid longer than the samples in Figure 11, more damage took place within the sample. Increased damage allowed for more slip planes to be weakened, and upon fracture, the sample separated along these planes simultaneously.

The 3D images in Figures 13 and 14 have similar characteristics on the fracture surface. In the 33 times magnification images, both figures have arrows indicating the focal point and have multiple slip planes present. Further signs of corrosion, however, are present in the 500 times magnification images. Even though both of these samples fractured on multiple slip planes, there are also visible indentations on the fracture surface area. The indentations present differentiate these images from those in Figure 12, indicating that increased exposure time caused more damage to the 3D samples.

Figure 15 showed further signs of damage in the 3D images. There are no clearly defined slip planes on the fracture surface as in Figures 13 and 14, nor are there indentations from the sample losing mass as in Figures 10, 13, and 14. The images in Figure 15 contrast from these previous images in two ways. First, the surface area is partially smooth, but there are small ridges along the entire fracture surface area. These ridges indicate a significantly increased number of potential slip planes compared to the samples exposed to the corrosive environment for short periods of time. Second, there are visible holes in Figure 15, as indicated by the arrows, which are larger than in any 3D

fracture images exposed for less time in the sulfuric acid solution. These holes are only present in Figure 15, indicating that the sulfuric acid continues to damage the 3D samples as exposure time increases.

Up to this point, exposure time in the sulfuric acid solution has not made a dramatic impact on the mechanical properties (Figures 6 and 7) or the observed physical properties of the samples (Figures 10 through 15). However, in Figures 6 and 7, a substantial decrease in both tensile stress and strain occurred after 1680 hours of exposure time for the 3D samples, while these values for the TM samples remained nearly constant. Although some of this may have been caused by unintentionally torqueing the samples in the tensile test, substantial damage is observed in the fracture surface of the 3D samples in the bottom row of Figure 16. Deep jagged holes, which were not present in the corresponding images of Figure 15, show that the samples were clearly affected by the sulfuric acid solution. Mass loss is easily observed in both the 33 and 500 times magnification images of the 3D samples, unlike the TM samples, which show little difference to the corresponding images after time 0 in Figure 9. Particles of the 3D samples were able to be removed because the corrosive ions that penetrated the surface reacted chemically with the material of the sample, formed solid brittle compounds, and allowed these particles to break off when the samples were subjected to tensile testing. The largest holes formed were most likely caused by the manner of mechanical failure the 3D samples experienced. The tensile test then pulled the samples apart, and the brittle material separated since the samples experienced hydrogen embrittlement, which left the jagged formations visible in images of the 3D samples in Figure 16. Figure 4

supports this observation, as the 3D samples lost mass nearly three times faster than the TM samples.

Figure 17 shows the SEM images of the 3D and TM samples after the maximum exposure time of 2184 hours. Few differences exist between the TM images in Figure 17 and the control samples in Figure 9. Both fracture surfaces of the samples contain some small holes, but the observed frequency of these holes have minimal variation. Figure 3 supports this observation; minimal damage appeared on the surface of the TM samples after the 2184 hours of exposure time, so it makes sense that the bulk of the TM samples also show minimal effects of corrosion damage. These results also are supported by Figure 4, which shows that the TM samples lost a very small amount of mass over the length of the study.

The 3D samples after the 2184 hours of exposure time show extensive damage on the fracture surface. Similar to the 3D sample images in Figure 16, some very large particles are missing from the fracture surface, which were likely loosened through hydrogen embrittlement and removed through tensile testing of the samples. However, comparing the 1680 hour and 2184 hour exposure time images of the 3D samples reveal that the 2184 hour samples experienced more damage from corrosion than the 1680 hours of exposure samples. A much larger number of small holes within the fracture surface of the 2184 hours of exposure samples were present, indicating that the corrosive environment had a more damaging impact on the sample as exposure time increased. This trend is further supported by comparing the 2184 exposure time images (Figure 17) with the 1176 exposure time images (Figure 15), which did show more damage after longer exposure. The cross sectional area of the 3D sample in Figure 17 shows large pieces of

material are missing, as shown by the arrows. Localized areas of the sample were subjected to hydrogen embrittlement, and the chemical reaction that took place formed brittle solids within the sample. The brittle portions of the sample allowed for particles to break off and be removed following tensile testing, resulting in the large holes present.

The control images of the 3D samples after 0 hours of exposure (Figure 9) look completely different from the images in Figure 17. The cross sectional area of the 3D sample in Figure 9 shows a smooth fracture surface. A small number of holes are present, most of which measure between 5 and 10 microns in diameter; otherwise, no other distinguishable damage is observed. The cross sectional area of the 3D sample in Figure 17, however, shows significant signs of damage. The frequency and size of the holes present are larger than in Figure 9; the largest holes measure nearly 200 microns in diameter, and many more still measure between 50 and 100 microns. Hydrogen embrittlement allowed for the formation of brittle portions within the samples after extended exposure time in the sulfuric acid solution. These brittle portions in the sample were then removed upon tensile testing, resulting in the large holes observed in Figure 17.

5.0 Conclusions

Samples produced using three dimensional (3D) and traditionally manufactured (TM) production methods were hypothesized to respond differently to a chosen corrosive environment. The environment, a sulfuric acid solution of 0.75M, was chosen to mimic the environment capable of being produced by the metabolic processes of common microorganisms. Only the production method differed between the two groups of samples, as the dimensions of the samples were based on ASTM standards (Figure 1) and the samples were made from the same material, stainless steel 316L. The 3D samples produced using the Laser Powder Bed Fusion (LPBF) method had differences compared to their TM counterparts. The rough surface of the 3D parts, as seen in Figures 2 and 3, was more easily attacked by the corrosive ions than the smooth surface of the TM samples. This ease of attack allowed for more mass to be removed from the 3D samples (Figure 4) and, through the mechanism of hydrogen embrittlement, negatively impacted mechanical properties of the 3D samples such as stress and strain (Figures 6 and 7, respectively). The method of fracture also differed between the samples of each method of production. The TM samples experienced ductile fracture while the 3D samples experienced brittle fracture, supported by the stress-strain curves in Figure 8.

Further evidence of the damage caused by the corrosive ions is observed in the Scanning Electron Microscope (SEM) images taken of the fracture surfaces of the samples after measured amounts of exposure time. Initially, there were differences in the surface area of the fracture surface between the 3D and TM samples. The large fracture area surface of the 3D samples along with the lower values of strain were evidence that these samples experienced brittle fracture. The TM samples saw a reduction in the

fracture surface area and had strain values more than twice as large as their 3D counterparts, indicating that the TM samples experienced ductile fracture. Production method differences caused the 3D samples to have increased residual stress, which also caused them to experience brittle fracture instead of ductile fracture like the TM samples. Though the type of fracture did not change between sample types or with prolonged exposure, the effect of the corrosive ions could be seen by the features observed on the fracture surface of the samples. As exposure time increased, minimal changes were seen between the TM samples; more holes on the fracture surface were present, but overall the appearance saw little change between time 0 and the maximum 2184 hours of exposure time. The sulfuric acid did not have an immediate impact on the 3D samples either. However, after extended exposure of 1680 hours, dramatic signs of corrosion and mass loss were observed. The large particles that were removed from the sample after tensile testing were only able to be removed because corrosive ions caused localized brittle precipitates to form through the mechanism of hydrogen embrittlement. Upon tensile testing, these areas attributed to the weakness of the material and promoted mass loss when fracture occurred.

The control images of both sample types show minimal defects on the fracture surface; only a small number of shallow holes are observed. After 2184 hours of exposure, the fracture surface of the TM samples showed no significant differences with the control images of the same production method. The 3D samples, however, exhibit easily observable signs of damage on the fracture surface after 2184 hours of exposure time. The 3D fracture surfaces in Figures 16 and 17 have dramatically different features than the fracture surface of the 3D samples in Figure 9 prior to any exposure. Particles

are missing along the jagged fracture surface, induced by the brittle precipitates that formed and allowed for the removal of mass from the bulk of the 3D samples during tensile testing.

6.0 Future Work and Recommendations

Future work regarding this subject would include analysis of different materials under the same conditions. As stainless steel is relatively resistant to corrosion because of the alloying elements present, the effects were somewhat difficult to measure. The differences between production methods of mass loss and the resulting changes in mechanical properties were relatively small. If a material more susceptible to corrosion was used, such as other more common grades of steel, then the differences could be observed more easily. Using different grades of steel would likely increase the effects of hydrogen embrittlement without the corrosion resistant alloying elements present in the 316L grade stainless steel used in this study. These more pronounced impacts on mechanical properties of the different grades could increase the understanding of the hydrogen embrittlement mechanism on steel samples.

Another possible route for additional experimentation would be to choose either a different concentration of sulfuric acid or to use a different corrosive solution. TM and 3D parts could be placed in a wide variety of environments, all of which would present different problems. The idea of 3D printing parts to be used in prosthetics or implants shows great promise as they can be designed with individual geometries depending on the patient. However, these parts would need to be tested under the conditions mimicking a human body and proven to still be effective before safe implementation. The human body presents a much different corrosive environment than the sulfuric acid solution used in this study. Hydrogen embrittlement will not be as able to occur, but a wide variety of other corrosive mechanisms could still potentially damage any 3D printed stainless steel parts used. The environment of the human body may even change with location; the

environment surrounding a leg, due to the presence of bone marrow, could be entirely different than the environment surrounding the skull, due to the presence of spinal fluid. All possible corrosive environments would need to be examined and properly tested before implementing the use of 3D printed prosthetics.

The Laser Powder Bed Fusion (LPBF) method used to produce the samples in this study is only one of many new emerging technologies in 3D printing. Other more complex methods of 3D printed materials have still not been tested under corrosive environments. Additionally, more methods of 3D printing and improvements upon older methods are always being developed. Advancements in 3D printing are leading to wider understanding of different variables used in the printing process such as powder composition, laser scanning speed, and many others. With greater understanding of these variables, soon 3D printed parts will be produced with comparable densities to their TM counterparts. 3D printed parts as dense and potentially as smooth as TM parts could lead to 3D parts that share the same corrosion resistant properties as their TM counterparts. A more extensive study would compare the LPBF 3D printed samples to 3D printed parts of the same geometries but produced with a different method exposed to the same corrosive environment.

After examining the results of this study, the surface characteristics of the samples caused by their respective production methods appear to have the greatest impact on hydrogen diffusion within the samples. This hypothesis comes from the findings in this study which support that density and porosity of samples using both of these production methods are relatively constant. A future study could attempt to determine the validity of this hypothesis by administering a similar surface treatment to samples of both

production methods. For example, grinding the surface of both TM and 3D samples with similar grades of sandpaper before exposure to the sulfuric acid would ensure the samples have the same surface features. Performing the tests described in this study with samples treated in this way would help determine if surface features are the dominating factor for hydrogen diffusing into the samples and causing damage through hydrogen embrittlement.

A further improvement upon this study could include a simple model attempting to predict the diffusion rate of hydrogen in both 3D and TM samples. Values for hydrogen diffusion in SS 316L are well documented, but such literature for 3D samples would likely be difficult to find. Laser scan speed, build rate, feed stock, and all other parameters in the 3D printing process would affect the diffusion rate; therefore, experimental data would need to be obtained to progress the model. The molarity of the corrosive solution used would be measured before and after sample exposure. The difference in molarity along with the known surface area of the samples could then be used to calculate the number of corrosive ions which penetrated the samples. Fick's Law could then be applied using the data obtained from samples of both production methods. A relationship could then be established between the diffusion of hydrogen into the samples and the resulting mass loss or changes in mechanical properties.

Controlling the corrosive environment for this study was challenging. Because the samples were placed in such large dishes to keep the samples separated by production method, large amounts of the sulfuric acid had to be produced each week. Sealing the dishes with plastic wrap was also challenging, as it was difficult to obtain a similar seal each week when the solution was replaced. In the future, splitting up the samples into

smaller groups would have been easier to work with. Using smaller dishes would have allowed for the sulfuric acid solution to be split up into smaller portions. This would minimize the variability of the ion concentration; using the large dishes could have allowed areas of higher and lower concentrations to form and corrode the samples at slightly different rates. Also, using containers with lids would cut down the variability in sealing the large dish each week to ensure that the solution did not evaporate. Keeping these ions in solution may increase the amount of damage the samples sustain, allowing for more observable differences on the surface of the samples as well as the fracture surface following tensile testing.

Obtaining images on the SEM was also challenging for some of the 3D samples. Brittle fractures of these samples sometimes occurred at steep angles, making it difficult to obtain focus on the desired surface features. This made comparisons of the surface features between samples with the same amount of exposure time less reliable. Future work would take multiple images of the sample with steep fracture surfaces at higher magnifications in order to make more accurate comparisons of fracture surface features.

Loading the samples on the INSTRON for tensile testing caused challenges as well. If any torque was inadvertently placed on the samples when loading it into the grips, the resulting data from breaking the samples would be skewed. Added torque could cause the tensile stress and the strain of a sample to be lower than their true values. The grips of the samples could be designed to allow for pins to be put through them instead of having to manually tighten the clams onto the samples. This would theoretically make sure that there is no additional torque when the samples are being fractured. An additional measure could be to use hydraulic grips to hold the samples during tensile

testing. Even with the samples that did not deviate as much as the 3D samples after 1680 hours of exposure time, there was some torque applied to all samples tested. Eliminating torque with the use of hydraulic grips would likely increase the recorded tensile strength values for all samples. Additionally, the difference observed between the tensile strength of the TM samples and the 3D samples would likely increase as well.

7.0 References

1. Nutting, Jack, and E.F. Wondris. "Steel." Encyclopedia Britannica. July 15, 2016. https://www.britannica.com/technology/steel.

2. Ashby, Michael F. & Jones, David R. H. (1992) [1986]. Engineering Materials 2 (with corrections ed.). Oxford: Pergamon Press.

3. Borgioli, Francesca, Emanuele Galvanetto, and Tiberio Bacci. 2016. "Low temperature nitriding of AISI 300 and 200 series austenitic stainless steels." *Vacuum* 127, 51-60.

4. McCafferty, E. *Introduction to corrosion science*. New York: Springer, 2010.

5. Jeffus, Larry F., and Jon Cookson. *Welding: principles and applications*. Clifton Park, NY: Thomson, 2004.

6. DeGarmo, E. Paul, J. Temple. Black, and Ronald A. Kohser. *Materials and Processes in Manufacturing* . Barcelona: Reverté, 2002.

7. Callister, William D., and David G. Rethwisch. *Materials science and engineering: an introduction*. Hoboken: John Wiley, 2014.

8. Shankar Rao, V., and L. Singhal. 2009. "Corrosion behavior and passive film chemistry of 216L stainless steel in sulphuric acid." *Journal Of Materials Science* 44, no. 9: 2327-2333.

9. Oberg, Erik, Franklin Day Jones, Holbrook Lynedon Horton, Henry H. Ryffel, and Christopher J. McCauley. *Machinery's handbook: a reference book for the mechanical engineer, designer, manufacturing engineer, draftsman, toolmaker, and machinist*. South Norwalk, CT: Industrial Press, 2016.

10. Askeland, Donald R., and Wendelin J. Wright. *The science and engineering of materials*. Boston, MA: Cengage Learning, 2016.

11. H. Alves, D. C. Agarwall, and H. Werner. 2006. "Alloys Suitable for Phosphoric Acid Applications," in NACE International, San Diego.

12. Zhong, Yuan, Leifeng Liu, Stefan Wikman, Daqing Cui, and Zhijian Shen. 2016. "Intragranular cellular segregation network structure strengthening 316L stainless

steel prepared by selective laser melting." *Journal Of Nuclear Materials* 470, 170-178.

13. Prem Ananth, K., A. Joseph Nathanael, Sujin P. Jose, Tae Hwan Oh, and D. Mangalaraj. 2016. "A novel silica nanotube reinforced ionic incorporated hydroxyapatite composite coating on polypyrrole coated 316L SS for implant application." Materials Science & Engineering: C 59, 1110-1124.

14. Utkin, I., I. Frantov, and D. Domov. 2015. "Effect of Chromium and Nickel on Heat-Affected Zone Properties with Welding of X70 Strength Category Niobium-Containing Steels." *Metallurgist* 59, no. 7/8: 590-596.

15. Dong, Lijin, Qunjia Peng, En-Hou Han, Wei Ke, and Lei Wang. 2016. "Stress corrosion cracking in the heat affected zone of a stainless steel 308L-316L weld joint in primary water." *Corrosion Science* 107, 172-181.

16. D. Manfredi, F. Calignano, M. Kirshnan, R. Canali, E. P. Ambrosio, S. Biamino, D. Ugues, and M. Pavese. 2014. “Additive Manufacturing of Al Alloys and Aluminum Matrix Composites (AMCs).,” in Light Metal Alloys Applications, InTech, p. Chapter 1.

17. W. Gao, Y. Zhang, D. Ramanujan, K. Ramani, Y. Chen, C. B. Williams, C. C. L. Wang, Y. C. Shin. 2015. “The Status, Challenges, and Future of Additive Manufacturing in Engineering.,” Computer-Aided Design, vol 69, p. 65-89.

18. Yadroitsev, I., A. Gusarov, I. Yadroitsava, and I. Smurov. 2010. "Single track formation in selective laser melting of metal powders." *Journal Of Materials Processing Technology* 210, no. 12: 1624-1631.

19. Kamath, Chandrika, Bassem El-dasher, Gilbert Gallegos, Wayne King, and Aaron Sisto. 2014. "Density of additively-manufactured, 316L SS parts using laser powder-bed fusion at powers up to 400 W." *International Journal Of Advanced Manufacturing Technology* 74, no. 1-4: 65-78.

20. Zhang, Baicheng, Lucas Dembinski, and Christian Coddet. 2013. "The study of the laser parameters and environment variables effect on mechanical properties of high compact parts elaborated by selective laser melting 316L powder." *Materials Science & Engineering: A* 584, 21-31.

21. Lykov, P., S. Sapozhnikov, I. Shulev, D. Zherebtsov, and R. Abdrakhimov. 2016. "Composite Micropowders for Selective Laser Sintering." *Metallurgist* 59, no. 9/10: 851-855.

22. Li, Ruidi, Yusheng Shi, Zhigang Wang, Li Wang, Jinhui Liu, and Wei Jiang. 2010. "Densification behavior of gas and water atomized 316L stainless steel powder during selective laser melting." *Applied Surface Science* 256, no. 13: 4350-4356.

23. R, Rai, Elmer J W, Palmer T A, and DebRoy T. 2007. "Heat transfer and fluid flow during keyhole mode laser welding of tantalum, Ti-6Al-4V, 304L stainless steel and vanadium." *Journal Of Physics: D Applied Physics* 40, no. 18: 5753-5766.

24. Simchi, A. 2006. "Direct laser sintering of metal powders: Mechanism, kinetics and microstructural features." *Materials Science & Engineering: A* 428, no. 1/2: 148-158.

25. Cherry, J., H. Davies, S. Mehmood, N. Lavery, S. Brown, and J. Sienz. 2015. "Investigation into the effect of process parameters on microstructural and physical properties of 316L stainless steel parts by selective laser melting." *International Journal Of Advanced Manufacturing Technology* 76, no. 5-8: 869-879.

26. P. Mercelis, J.P. Kruth. 2016. “Residual Stresses in Selective Laser Sintering and Selective Laser Melting,” Rapid Prototyping, vol. 470, p. 170.

27. Kruth J. P., Badrossamay M., Yasa E., Deckers J., Thijs L., Humbeeck J. V. 2010.“Part and material properties in selective laser melting of metals”, in 16th International symposium on electromachining (ISEM XVI), doi: https://lirias.kuleuven.be/handle/123456789/265815

28. Mine, Yoji, Nobuaki Horita, Zenji Horita, and Kazuki Takashima. 2017. "Effect of ultrafine grain refinement on hydrogen embrittlement of metastable austenitic stainless steel." *International Journal Of Hydrogen Energy* 42, no. 22: 15415-15425.

29. Matsuo, Takashi, Junichiro Yamabe, and Saburo Matsuoka. 2014. "Effects of hydrogen on tensile properties and fracture surface morphologies of Type 316L stainless steel." *International Journal Of Hydrogen Energy* 39, no. 7: 3542-3551.

30. Mine, Yoji, and Takashi Kimoto. 2011. "Hydrogen uptake in austenitic stainless steels by exposure to gaseous hydrogen and its effect on tensile deformation." *Corrosion Science* 53, no. 8: 2619-2629.

31. Terada, Maysa, Angelo Oliveira Zimmermann, Hugo Sandim, Isolda Costa, and Angelo Padilha. 2011. "Corrosion behavior of Eurofer 97 and ODS-Eurofer alloys compared to traditional stainless steels." *Journal Of Applied Electrochemistry* 41, no. 8: 951-959.

32. Naiming, Lin, Liu Qiang, Zou Jiaojuan, Guo Junwen, Li Dali, Yuan Shuo, Ma Yong, Wang Zhenxia, Wang Zhihua, and Tang Bin. 2016. "Surface Texturing-Plasma Nitriding Duplex Treatment for Improving Tribological Performance of AISI 316 Stainless Steel." *Materials (1996-1944)* 9, no. 11: 1-26.

33. Borgioli, F., A. Fossati, G. Matassini, E. Galvanetto, and T. Bacci. 2010. "Low temperature glow-discharge nitriding of a low nickel austenitic stainless steel." *Surface & Coatings Technology* 204, no. 21/22: 3410-3417.

34. Okabe, Satoshi, Mitsunori Odagiri, Tsukasa Ito, and Hisashi Satoh. 2007. "Succession of Sulfur-Oxidizing Bacteria in the Microbial Community on Corroding Concrete in Sewer Systems." *Applied & Environmental Microbiology* 73, no. 3: 971-980.

35. Ma, C.P., Y.C. Guan, and W. Zhou. 2017. "Laser polishing of additive manufactured Ti alloys." Optics & Lasers In Engineering 93, p. 171-177.

36. Dierksen, Detlef, Petra Kühner, Andreas Kappler, and Klaus G. Nickel. 2011. "Microbial corrosion of silicon nitride ceramics by sulphuric acid producing bacteria Acidithiobacillus ferrooxidans." *Journal Of The European Ceramic Society* 31, no. 6: 1177-1185.

37. Usher, K.M., A.H. Kaksonen, D. Bouquet, K.Y. Cheng, Y. Geste, P.G. Chapman, and C.D. Johnston. 2015. "The role of bacterial communities and carbon dioxide on the corrosion of steel." *Corrosion Science* 98, 354-365.

38. Chandrasatheesh, C., J. Jayapriya, R.P. George, and U. Kamachi Mudali. 2014. "Detection and analysis of microbiologically influenced corrosion of 316 L stainless steel with electrochemical noise technique." *Engineering Failure Analysis* 42, 133-142.

39. Kang, K.W., M.D. Pereda, M.E. Canafoglia, P. Bilmes, C. Llorente, and R. Bonetto. 2012. "Uncertainty studies of topographical measurements on steel surface corrosion by 3D scanning electron microscopy." *Micron* 43, no. 2/3: p. 387-395.

40. Brandon, David G., and Wayne D. Kaplan. *Microstructural characterization of materials*. Chichester: Wiley, 2006.

41. Ford, Brian J., Savile Bradbury, and David C. Joy. "Scanning electron microscope (SEM)." Encyclopædia Britannica. May 17, 2016. https://www.britannica.com/technology/scanning-electron-microscope.

42. Yang, Nancy, J. Yee, B. Zheng, K. Gaiser, T. Reynolds, L. Clemon, W. Lu, J. Schoenung, and E. Lavernia. 2017. "Process-Structure-Property Relationships for 316L Stainless Steel Fabricated by Additive Manufacturing and Its Implication for Component Engineering." Journal Of Thermal Spray Technology 26, no. 4: 610-626.

43. Dongare, Sujitkumar T. E. Sparks, J. Newkirk and Frank Liou. 2014. “A Mechanical Testing Methodology for Metal Additive Manufacturing Processes.” Missouri University of Science and Technology, p. 224-243